2017

Effect of Convection Associated with Cross-Section Change During Directional Solidification of Binary Alloys on Dendritic Array Morphology and Macrosegregation

Masoud Ghods
Cleveland State University

Effect of Convection Associated with Cross-section Change during Directional Solidification of Binary Alloys on Dendritic Array Morphology and Macrosegregation

Masoud Ghods

Bachelor of Science in Chemical Engineering

Amirkabir University of Technology, Tehran, Iran. May 2009

Master of Science in Chemical Engineering

Sharif University of Technology, Tehran, Iran. May 2012

Submitted in Partial Fulfillment of the Requirements for the Doctor of Engineering Degree in the College of Graduate Studies

Cleveland State University

July 2017

We hereby approve this dissertation
of
Masoud Ghods

Candidate for the Doctor of Engineering in Chemical Engineering

for the Department of
Chemical and Biomedical Engineering

And

CLEVELAND STATE UNIVERSITY'S
College of Graduate Studies by

_____

Surendra Tewari, Ph.D
Dissertation Committee Chairperson
Department of Chemical and Biomedical Engineering, Cleveland State University

_____

Jorge E. Gatica, Ph.D
Department of Chemical and Biomedical Engineering, Cleveland State University

_____

Orhan Talu Ph.D
Department of Chemical and Biomedical Engineering, Cleveland State University

_____

Rolf Lustig, Ph.D
Department of Chemical and Biomedical Engineering, Cleveland State University

_____

Kiril A. Streletzky, Ph.D
Department of Physics, Cleveland State University

Date of Defense: July-06-2017

This student has fulfilled all requirements for the Doctor of Engineering degree.

_____

Chandra Kothapalli, Ph.D.
Doctoral Program Director, Cleveland State University

Acknowledgment

I will always be indebted to Prof. Surendra N. Tewari who has always been ready to help as my advisor, and taught me how to walk through difficulties in this research. I would like to thank Luke Johnson who helped me at the very initial steps of this research. I would also like to acknowledge the work of Mark Lauer, former PhD student at The University of Arizona, which provided a better insight about this research for me. I am grateful of collaborative work with Dr. Richard N. Grugel from NASA Marshal Space Flight Center. I am thankful of David Epperly from the Washkewicz College of Engineering at Cleveland State University who helped me in the preparing the specimens.

I would like to thank my love and best friend, Saeedeh, who encouraged me throughout this long journey, and tried to show me different perspectives of life. And finally, I am thankful of my cute and loving cat, Pooneh, who has been selflessly spreading joy to my life!

Support from National Aeronautics and Space Administration (NASA) Grants NNX14AJ73G, NX10AV40G and NNX14AM18G is gratefully acknowledged.

Effect of Convection Associated with Cross-section Change during Directional Solidification of Binary Alloys on Dendritic Array Morphology and Macrosegregation

Masoud Ghods

Abstract

This dissertation explores the role of different types of convection on macrosegregation and on dendritic array morphology of two aluminum alloys directionally solidified through cylindrical graphite molds having both cross-section decrease and increase. Al- 19 wt. % Cu and Al-7 wt. % Si alloys were directionally solidified at two growth speed of 10 and 29.1 μm s^{-1} and examined for longitudinal and radial macrosegregation, and for primary dendrite spacing and dendrite trunk diameter.

Directional solidification of these alloys through constant cross-section showed clustering of primary dendrites and parabolic-shaped radial macrosegregation profile, indicative of "steepling convection" in the mushy-zone. The degree of radial macrosegregation increased with decreased growth speed. The Al- 19 wt. % Cu samples, grown under similar conditions as Al-7 wt. % Si, showed more radial macrosegregation because of more intense "stepling convection" caused by their one order of magnitude larger coefficient of solutal expansion.

Positive macrosegregation right before, followed by negative macrosegregation right after an abrupt cross-section decrease (from 9.5 mm diameter to 3.2 mm diameter),

were observed in both alloys; this is because of the combined effect of thermosolutal convection and area-change-driven shrinkage flow in the contraction region. The degree of macrosegregation was found to be higher in the Al- 19 wt. % Cu samples. Strong area-change-driven shrinkage flow changes the parabolic-shape radial macrosegregation in the larger diameter section before contraction to "S-shaped" profile. But in the smaller diameter section after the contraction very low degree of radial macrosegregation was found.

The samples solidified through an abrupt cross-section increase (from 3.2 mm diameter to 9.5 mm diameter) showed negative macrosegregation right after the cross-section increase on the expansion platform. During the transition to steady-state after the expansion, radial macrosegregation profile in locations close to the expansion was found to be "S-shaped". This is attributed to the redistribution of solute-rich liquid ahead of the mushy-zone as it transitions from the narrow portion below into the large diameter portion above.

Solutal remelting and fragmentation of dendrite branches, and floating of these fragmented pieces appear to be responsible for spurious grains formation in Al- 19 wt. % Cu samples after the cross-section expansion. New grain formation was not observed in Al-7 wt. % Si in similar locations; it is believed that this is due to the sinking of the fragmented dendrite branches in this alloy.

Experimentally observed radial and axial macrosegregations agree well with the results obtained from the numerical simulations carried out by Dr. Mark Lauer and Prof. David R. Poirier at the University of Arizona.

Trunk Diameter (TD) of dendritic array appears to respond more readily to the changing growth conditions as compared to the Nearest Neighbor Spacing (NNS) of primary dendrites.

Table of Contents

List of Tables

List of Figures

Chapter I

Background and Review of Literature

1.1 Conventional Casting

The purpose of this research is to better understand the role of convection during metallic alloys solidification. Convection is important because it adversely influences the microstructure generating defects, and produces chemical inhomogeneity over length scales larger than primary dendrite spacing called “macrosegregation.” These defects degrade the mechanical properties of solidified components. In conventional alloy casting, hot alloy liquid is poured into a cold mold; so, heat transfer and consequently thermal gradients and solidification rate are determined by the mold material and geometry. As the hot melt comes in contact with the cold mold, solidification starts and forms many equiaxed grains. Those grains which are favorably oriented in the heat extraction direction grow at the expense of misoriented ones creating a region of

columnar grains. As the rest of the melt cools further, it gets undercooled below its liquidus temperature, nucleating new equiaxed grains. The final microstructure, therefore, consists of equiaxed grains at the ingot surface, followed by columnar grains and then finally equiaxed grains in the interior of ingot, as shown schematically in Figure 1.

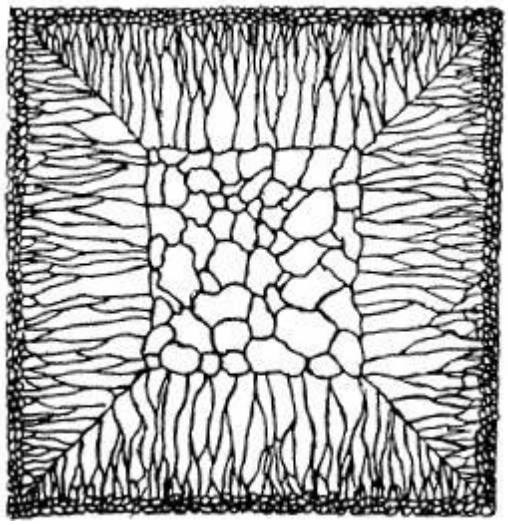

Figure 1: Schematic representation of columnar to equiaxed grain transition in conventional castings [1].

1.2. Directional Solidification

During directional solidification, the alloy is melted and then slowly solidified from one end of the ingot to the other end resulting in columnar grains aligned with the growth direction. In this method, the alloy kept in a crucible is inserted into a furnace assembly which consists of hot zone above and a cold zone below with an adiabatic zone in between. Purpose of the adiabatic zone is to minimize radial heat loss and ensure positive thermal gradient along the sample length. Sample portion above the liquidus temperature (T_l) of the alloy, for example T_l= 614 ^oC for Al-7 wt. % Si alloy (Figure 2(b)), is melted, and that below the eutectic temperature (T_E= 577 ^oC) is solid. The

sample portion in between T_l and T_E contains a mixture of solid (α-phase) and liquid and is called "mushy-zone." The cone-like feature drawn on the schematic of a phase diagram in fig. 2(a) represents a typical mushy-zone. Because of the dendrite tip undercooling (due to the tip curvature), the temperature right at the tip is slightly lower than the liquidus temperature corresponding to the bulk liquid composition. Therefore, the concentration of the liquid in contact with the tip is C_{tip}, which is slightly larger than C_0 (see fig. 2(a)). The crucible containing the alloy is withdrawn from the furnace hot-zone towards the cold-zone below at a constant speed to carry out directional solidification of entire sample length at constant growth speed (R) and thermal gradient at the liquid-mushy zone interface (G_l).

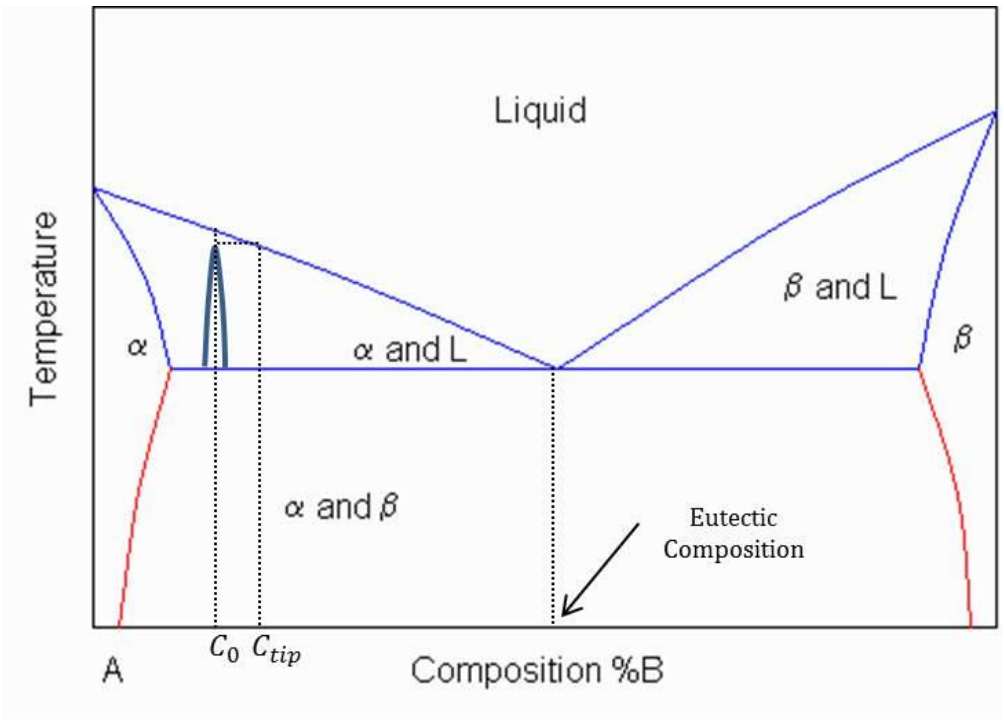

(a)

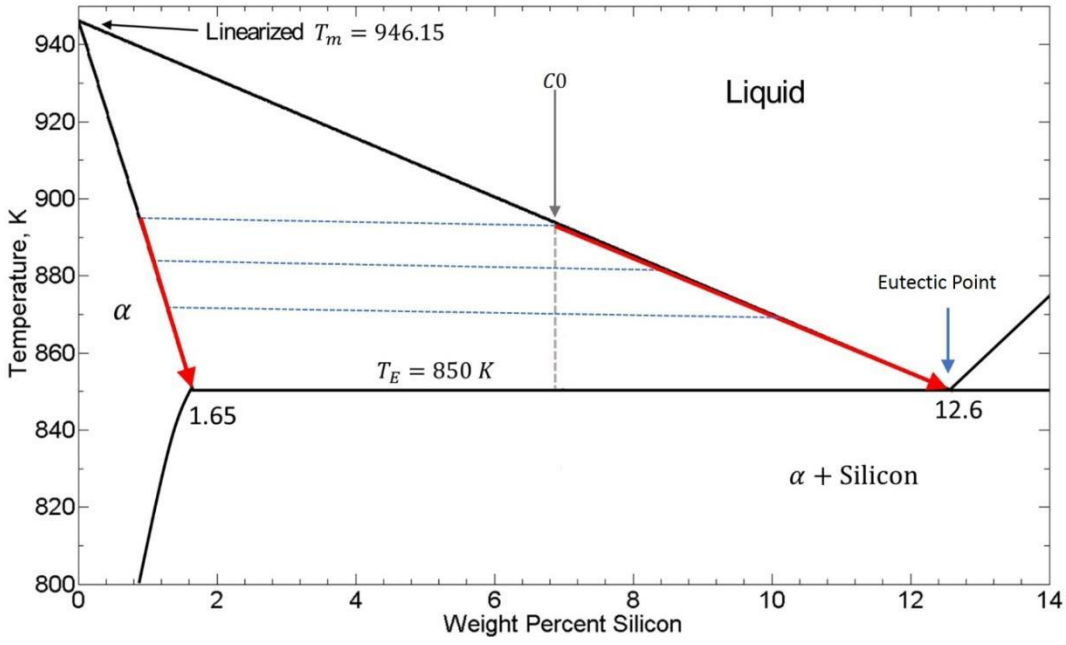

(b)

Figure 2: (a) is a schematic of the binary eutectic phase diagram; the cone-like feature represents a typical mushy-zone. (b) is the partial equilibrium Al-Si phase diagram showing the melting point of aluminum Tm, different phases, the eutectic point, and solidification path in the liquid and solid phase for a typical alloy with C0 initial composition [J. L. Murray and A. J. McAlister: Bull. Alloy Phase Diagram, vol. 5, no. 1, 74 (1984).].

1.2 Dendritic Array Morphology during Directional Solidification

The mushy-zone contains an array of aligned branched "tree"-like solid features called dendrites with liquid occupying the interdendritic space between the liquidus and the eutectic temperature of the alloy. Typical dendrites in the mushy-zone are shown in figure 3 for a transparent organic (succinonitrile-water) alloy system which simulates the mushy-zone in metallic alloys. The *primary dendrites* have four orthogonal side branches called *secondary arms*, which can have their own four-fold orthogonal side-arms (tertiary branches). The composition of the interdendritic liquid in the mushy-zone varies from C_{tip}, slightly higher than the overall solute content of the sample (C_0) because of the tip curvature, at the array tips to eutectic concentration, C_E, at the base of the mushy-zone.

Several morphological properties are defined to characterize the mushy-zone microstructures; the diameter of primary dendrites is called *trunk diameter*, Φ, and their spacing is called *primary dendrite arm spacing*, λ. The size and distribution of these morphological features in the microstructure depend upon the local growth conditions and thermophysical properties of the alloy, and have direct correlation with the chemical and mechanical properties of the solidified component. Solidification of the liquid at the base of the mushy-zone results in a eutectic solid having alternating plates or fibers of the two phases in equilibrium at the eutectic temperature; for example aluminum-rich α, and Si in the case of Al-7Si alloy.

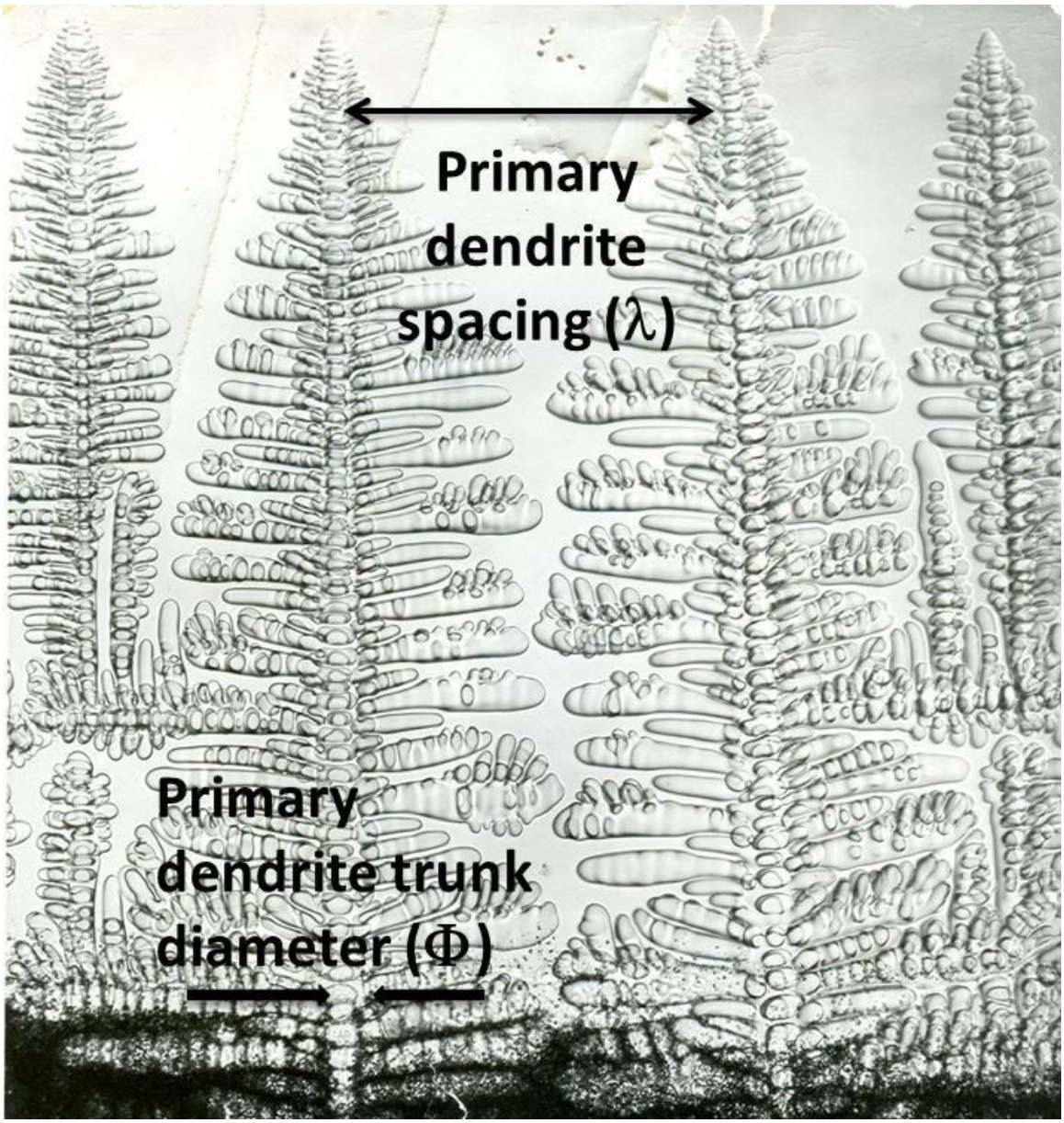

Figure 3: Mushy-zone of the Succinonitrile – 9 wt. % Water "Transparent alloy" directionally solidified (~ 5 μm s-1, ~30 Kcm-1) (Dr. Grugel, NASA-MSFC)

The ratio of the concentration in the solid, C_s, to that in the liquid at the liquid-solid interface, C_l, at any temperature is called equilibrium partition ratio, k. If rapid diffusion of solute in both liquid and solid phases is assumed then the weight fraction of the liquid phase, f_l, at any temperature in the mushy-zone can be found from the

equilibrium phase diagram using the inverse lever rule. In this case volume fraction liquid is:

$$f_l = \frac{C_0 - kC_l}{C_l(1-k)} \qquad (1)$$

However, the diffusion coefficient of solute in the solid phase is usually 4 orders of magnitude smaller than that in the liquid phase, therefore no diffusion in solid and perfect diffusion in liquid is more valid assumption. In this case, the following Scheil [2] or Gulliver-Scheil [3] relationship describes the microsegregation.

$$f_l = \left(\frac{C_l}{C_0}\right)^{\left(\frac{1}{k-1}\right)} \qquad (2)$$

1.3 Flows During Directional Solidification

The role of convection as it pertains to solidification through a change in cross-section has not only scientific merit and has never been reported before, but it is also relevant to the important technology of producing directionally solidified castings. First stage turbine blades are the most crucial rotating components of gas turbine engines in determining the fuel efficiency and performance of the engine. Hot combustion gases from the combustion chamber first hit the first stage turbine blades attached to a disk; the disk begins to rotate. This rotation is transmitted via its shaft to other portions of the engine. For example, it keeps the large fan-blades in front of the engine rotating which generates most of the engine thrust. A typical first stage turbine blade is shown in figure 4. The thicker root-section at the bottom fits into the turbine disk, and the curved palm-like thin airfoil portion above takes on the impact from the high temperature hot velocity

gases. The bright and dark features running along the length of the blade are the grains which have been purposely aligned along the blade axis to improve the blade life. The circular view in the middle shows at higher magnification, what the dendrites look like on the transverse section of the blade along its length. In high performance engines, the multiple grain boundaries are totally eliminated and the entire blade is made as one single grain with its [100] orientation parallel to the blade length without the presence of any misoriented or "spurious" grains. Presence of spurious misaligned grains is highly detrimental to the elevated temperature mechanical properties and is the principal cause of rejection of these blades by the manufacturers. In addition, the grain selector at the bottom and the platforms at the root and tip of blade introduce other section changes. Defects that lead to rejecting a directionally solidified turbine blade after its manufacture are grain misalignment, low angle grain boundaries, spurious grains, and freckles; all of these are believed to be related to the combined effects of shrinkage-driven convection and thermosolutal convection at the cross-sectional changes. Reed [4] reports scrap rates of around 30% for first-stage turbine blade castings.

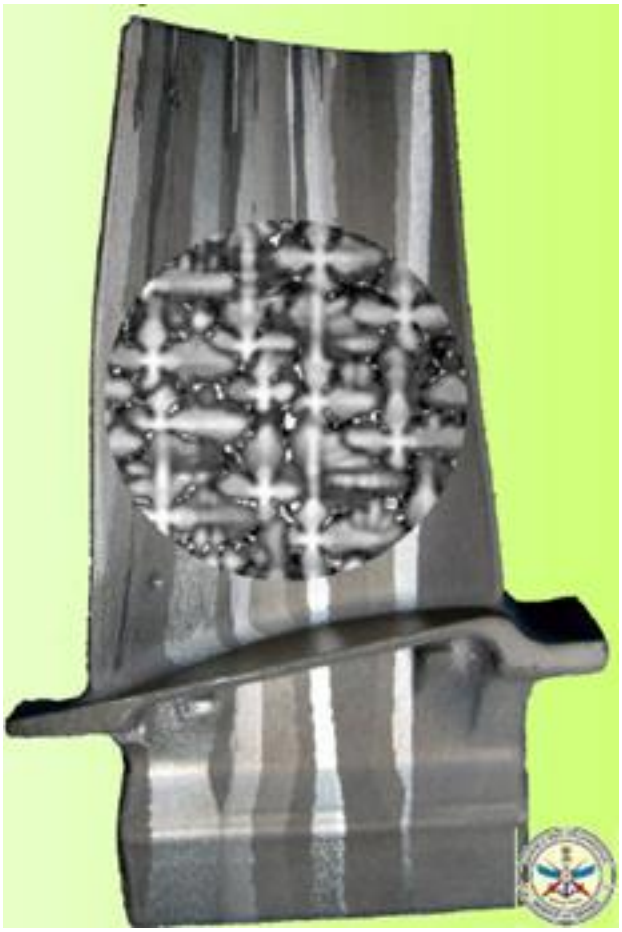

Figure 4: A typical gas turbine engine blade (DMRL-ICSSP-6-Hyderabad). The bright and dark features running along the length of the blade are the grains. The circular view in the middle shows at higher magnification, what the dendrites look like on the transverse section of the blade along its length

There are different possibilities for the interdendritic liquid response to gravity force depending upon how the melt density varies with temperature and solute concentration. As shown schematically in figure 5, the thermal profile in the interdendritic melt is stabilizing against natural convection; hot temperature melt with lower density is above and lower temperature, higher density, melt is below. For alloys with partition coefficient, k, less than unity the maximum liquid concentration, C_E, is at the bottom of the mushy zone; it decreases upwards to the tips where the concentration is C_{tip}. If the decreasing solute content in the liquid results in the decreasing density, which is the case in alloys where the solute density is higher than the solvent's (for example Al-

19% Cu), then the interdendritic composition gradient is *stabilizing* against natural convection (Figure 5(a)). But, if the solute density is smaller than the solvent's, for example in Pb-6 wt. % Sb, then solute-rich liquid at the base of the mushy zone is lighter than low solute liquid at the array tips (Figure 5(b)); this density inversion is destabilizing and can lead to natural convection.

In the case where combined thermal and solutal effects create a density inversion, as depicted in figure 5(b), the interdendritic thermosolutal convection ensues which results in chemical inhomogeneity or so-called macrosegregation [1, 5-8]. Under severe density inversion, induced convection of this type in some alloys can create highly detrimental defects called "freckles" [8-10].

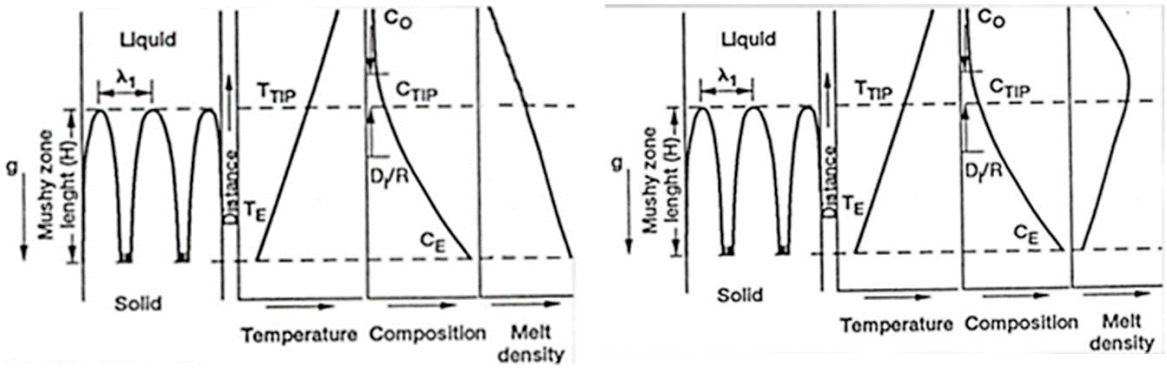

Figure 5: Schematic of temperature, concentration and density profiles in the interdendritic liquid; (a) is for solutally stabilizing liquid, and (b) is for solutally destabilizing liquid.

One would not expect natural convection to occur for growth conditions which are stabilizing against natural convection during upwards directional solidification. But as explained below there are three types of fluid flows present during directional solidification. During directional solidification involving a section increase or decrease

the behavior of these flows and their interaction with each other will be expected to change and influence the solidification process in the vicinity of section change.

The first type of flow present is *thermal convection*. The difference between the thermal conductivity of the mold and the alloy in one hand, and two-fold increase in the thermal conductivity of the solid phase forming from the melt as solidification proceeds on the other, generate radial thermal gradient. This initiates thermal flows in the all-liquid region above the mushy-zone such that the hotter melt near the mold walls flows upward while the cooler melt in the interior flows downward; these thermal convection cells are indicated as two dashed circular arrows in figure 6(a). Cooler temperatures in the central region and downwards flow of the liquid there favor primary dendrite growth; consequently, primary dendrites grow slightly ahead of their neighboring dendrites there. This results in the denser liquid at the tip of the leading dendrites, with C_{tip} concentration which is slightly higher than C_0, to flow sideways and downwards towards the tips of lagging neighbors, where the less dense liquid with C_0 concentration exists (see fig. (a)). This inhibits the growth of lagging dendrites even more. This flow is called "Steepling" type of *thermosolutal convection* and is the second type of fluid flow present during directional solidification of solutally stabilizing alloys. As the solidification proceeds this flow gets intensified and creates a mushy zone-liquid interface which instead of being flat is convex towards the all-liquid region above, or in another word the mushy-zone becomes *steepled*. In the figure 6(a) the steepled mushy-zone is schematically shown (compare it with mushy-zone seen in figure 3 where all the primary dendrite tips are at the same level); corresponding thermosolutal flow is schematically denoted as dotted

arrows rolling over the mushy-zone; this type of fluid flow is also known as *steepling flow*.

As the interdendritic liquid freezes it occupies less volume, the liquid from the top of the mushy-zone flows towards the liquid-solid interface to feed this solidification shrinkage. This *shrinkage flow* always exists during directional solidification, irrespective of gravity level. The solid arrows pointing down in the figure 6(a) show this flow schematically.

During directional solidification involving a cross-section decrease, as the mushy-zone growing previously in a larger constant cross-section region below approaches the smaller cross-section region above, shrinkage flow intensity is expected to increase because the liquid from a narrower cross-section above has to feed the solidification shrinkage still happening in the larger diameter below; this flow is called *area-change-driven shrinkage flow*. The thick solid arrows in the smaller diameter section shown in figure 6(b) indicate this flow. The strength of thermal convection due to radial thermal gradients is expected to be less in the narrow portion of the mold as compared with that in the wider portion below. Small dashed circular arrows after the section-decrease in figure 6(b) represent thermal convection cells in this portion.

On the other hand, during directional solidification involving a cross-section increase, there is strong thermal convection within the all-liquid region above the section change, shown schematically by the circular dashed arrows in the figure 6(c). The shrinkage flow intensity, however, begins to decrease as the mushy-zone approaches the section-increase because now the liquid pool from the larger diameter section above feeds

the relatively less solidification shrinkage happening in the smaller diameter portion below. Small solid arrows in the figure 6(c) show this flow. The steepled mushy-zone and the corresponding thermosolutal flow in the narrow portion of the mold are also seen in the figure 6(c).

These flows, their interaction, and their effects on chemical inhomogeneity will be studied in detail in this research.

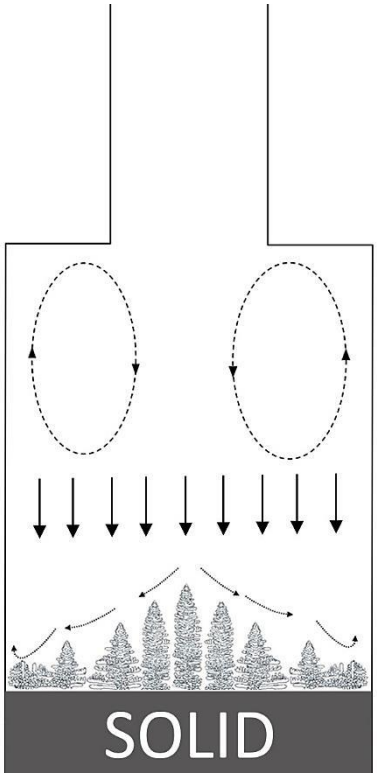

(a)

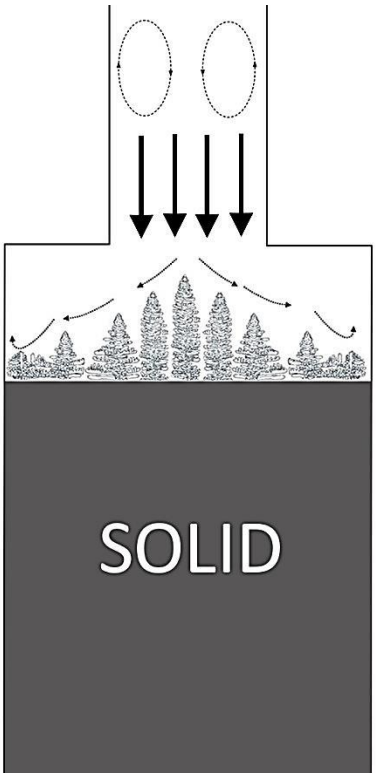

(b)

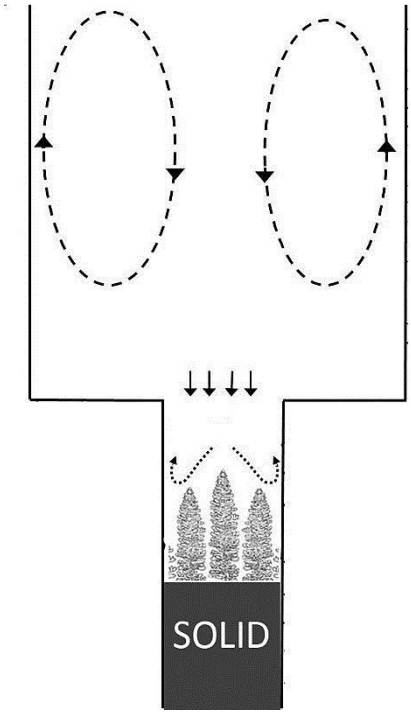

(c)

← Figure 6: Schematic of the mold with changing cross-section including the mushy-zone, thermal convection cells (dashed circular arrows), shrinkage flow (solid arrows) and thermosolutal convection (dotted arrows rolling over the mushy-zone); (a) is for when the mushy-zone is away from the contraction, (b) is for when the mushy-zone is approaching the contraction, and (c) is for when the mushy-zone is reaching the expansion.

1.5 Literature Review

1.5.1 Influence of Convection on Macrosegregation (constant cross-section area mold)

Steepling was first investigated by Burden et al. [11] where they presented the results of solidification of several hypoeutectic Al-Cu alloys. There is always some small radial thermal gradient, especially at low growth speeds, which starts the fluid flow; this flow advects the solute with itself and creates macrosegregation. There has been significant experimental works on steepling. Burden et al. [11] and McCartney and Hunt [12] performed experiments in Al-Cu alloys. Mason et al. [13] and Verhoeven et al. [14] investigated steepling using several lead alloys. Nguyen Thi et al. [15] and Billia et al. [16] published results showing steepling in Al-Ni and Al-Si alloys.

1.5.2 Influence of Convection on Dendrite Array Morphology (constant cross-section area mold)

Influence of convection on dendrite morphology has been examined by superimposing a shear flow that is transverse to the growth direction during solidification of transparent model alloys [17-21]. There have been efforts in comparing the microstructures of terrestrially solidified alloy samples with those grown in low-gravity [15, 22-23]; also by developing semi-quantitative formulations that qualitatively explain the discrepancy between observed primary spacing with those predicted from models which are based on purely diffusive transport [23-24]. The imposed shear flow

experiments showed that side-branching is enhanced upstream of the primary dendrites and suppressed downstream. Also, the primary spacing is significantly larger in the presence of shear flow. In these experiments, however, the wall effects distorted the array morphology and thus the true three-dimensional behavior of dendritic arrays was missed. An opposite effect is seen for metallic alloys; the low-gravity samples have spacings that are two to four times larger than the terrestrially grown samples [23]. All this strongly suggests that the changes of dendritic morphology resulting from transverse shear flows do not represent those that are associated with the thermosolutal convection during directional solidification.

1.5.3 Influence of cross-section-change-induced shrinkage convection during directional solidification on macrosegregation.

Macrosegregation accompanying directional solidification through cross-sectional changes was experimentally investigated several decades ago [24-27]; during that period, the associated fluid flow was modeled by considering only the shrinkage flow and multidimensionality of fluid flow was assessed only qualitatively. Since then there were computer simulations of macrosegregation at cross-sectional changes in multicomponent alloys [28-29]. The underlying solidification transport model of these simulations included both thermosolutal convection and shrinkage driven convection; no experimental work, however, was done.

Formation of defects due to solidification through cross-section change has been investigated by many authors. For example, formation of misoriented grains has been studied in superalloys, both experimentally and by numerical modeling [30, 31]. Coupled

finite element-cellular automaton model has been used to predict dendritic grain structures resulting from solidification through cross-section changes [30]. Here it was assumed that because of more efficient heat extraction associated with the platform corners, the melt there is locally undercooled resulting in nucleating new stray grains. This approach, however, ignores the thermosolutal or shrinkage driven convection associated with solidification through section change. Convective flows can remelt tertiary branches [32] which can become new grains.

Convective flows are well-known to produce "channel segregate" or freckles discussed before, often associated with directional solidification through cross-section change [33]. There are some studies that examined the effect of cross-section change on dendrite morphology [30, 34]. However, these used thin-slab shaped ampoules containing transparent analogue alloys, therefore do not represent the three-dimensional behavior of dendrite array, and do not account for thermosolutal convection. The effects of convection due to changing cross-section on the dendritic microstructure and array morphology have not been studied in metallic alloys, either experimentally or via modeling.

1.6 Purpose of This Research

As mentioned earlier, the imposed longitudinal thermal gradient results in the varying concentration in the interdendritic liquid; this affects the properties of the liquid, primarily its density. Any flow of the interdendritic liquid to regions with different temperatures results in macrosegregation, and could even initiate changes in the morphology of the dendritic array by remelting or inducing the local growth of primary α-phase. Interdendritic liquid flow can be started by forced convection, e.g. imposing

magnetic field or stirring the liquid, or through natural convection induced by the density differences due to temperature or concentration variations.

In this research, the effect of combined shrinkage and thermosolutal convection during directional solidification on well-designed alloy systems, experiencing cross-section change during the process, are investigated. In a microgravity environment, the thermosolutal convection will be mitigated. Thus, by comparing results from terrestrial directional solidification experiments with those from the samples solidified in microgravity, the role of thermosolutal and the shrinkage components in producing the chemical and the microstructural inhomogeneities in castings can be independently studied, which would enable the development of predictive tools. This work also produces benchmark solidification data which will be used for future space experiments design and comparison.

Chapter II

Experimental Procedure

2.1 Alloy Selection

Since the main purpose of this research is to explore the natural convection behavior and effects on the macrosegregation and the morphological properties of the dendritic microstructure, alloys should be selected such that their liquid phase show different response to buoyancy forces.

As described earlier, in a positive thermal gradient interdendritic liquid density (ρ) is a function of temperature and concentration; so it could be written as:

$$\rho = \rho(C, T) \tag{3}$$

therefore,

$$d\rho = \frac{\partial \rho(C,T)}{\partial T}\Big)_C dT + \frac{\partial \rho(C,T)}{\partial C}\Big)_T dC \tag{4}$$

β_T , coefficient of thermal expansion, and β_C , coefficient of solutal expansion are defined like:

$$\beta_T = \frac{1}{\rho_0}\frac{\partial \rho(C,T)}{\partial T})_C \quad (5)$$

and

$$\beta_C = \frac{1}{\rho_0}\frac{\partial \rho(C,T)}{\partial C})_T \quad (6)$$

So we could write Eq. (4)

$$\frac{d\rho}{\rho_0} = \beta_T dT + \beta_C dC \quad (7)$$

This expression shows how the density is correlated with thermal and solutal variations through β_C and β_T as materials properties.

Two binary alloy systems were selected to conduct directional solidification experiments, Al-19 wt. % Cu and Al- 7 wt. % Si. These systems have similar solidification shrinkage, but their solute densities as compared to their corresponding solvent densities are significantly different. In case of Al- 19 wt. % Cu alloy, density of copper, 8.02 g/cm^3, is much greater than that of aluminum, 2.375 g/cm^3, which means increasing solute content within the interdendritic liquid moving from the tips to the base of the mushy-zone drastically increases the melt density; this makes this system heavily stable with respect to buoyancy forces. As opposed to that in Al-7 wt. % Si alloy, density

of silicon is 2.57 g/cm^3, which is only slightly greater than that of aluminum; so, the density of solute-enriched liquid is very similar to that of the original liquid with C_0 concentration. The densities mentioned here are at the melting points of pure elements. Coefficient of solutal expansion and coefficient of thermal expansion for these alloys can be found in literature; Table I includes these values for alloys of our interest at their corresponding liquidus temperature.

Table I: Coefficient of Thermal Expansion and Coefficient of Solutal Expansion of Alloys of Interest [35-37]

	β_T (K^{-1})	β_C (% solute)$^{-1}$
Al- 19 wt% Cu	-1.85×10^{-4}	2.35×10^{-2}
Al- 7 wt% Si	-1.85×10^{-4}	1.3×10^{-3}

Negative thermal expansion coefficient of alloys means that increasing temperature along the sample length towards the top (gravity pointing down) will result in decreasing density; on the other hand, positive solutal expansion coefficient in Al-19Cu and Al-7Si would result in melt density increasing toward the bottom of mushy zone, the extent of increase being much larger in Al-19Cu than in Al-7Si. It implies that any flow caused by the variation of composition in the mushy-zone or the bulk liquid ahead, is much stronger in Al-19Cu as compared to that in Al-7Si.

2.2 Crucible and Sample Assembly

The as-cast Al-19Cu and Al-7Si feed rods used in these experiments were provided by the ALCOA technical center in Pittsburgh. They were made by induction melting of 99.99% Aluminum, 99.99% Silicon, and 99.99 % copper under an argon atmosphere, and then poured into copper molds to produce 30 cm long rods, 9 mm in diameter. The ALCOA technical center also chemically analyzed these rods for impurities.

Cylindrical graphite crucibles, shown in figure 7, machined such that they contained both an abrupt cross-section decrease and also an abrupt increase were used for the directional solidification of Al-19Cu and Al-7Si alloys. The crucibles were about 30 cm long and 1.9 cm outer diameter. They contained internal cylindrical cavity, 13 cm long 9.5 mm in diameter followed by a 5 cm long and 3.2 mm in diameter, which reverted back to the 9.5 mm in diameter for the remaining crucible length. Four chromel-alumel thermocouples were placed in groves machined on the outer surface of the crucibles along their length to record the temperature profile during directional solidification (figure 7).

Figure 7: Typical graphite crucible used for directional solidification experiments. The horizontal arrow shows the solidification direction, and small vertical arrows indicate the location of thermocouples used to record temperature data along the length of the samples.

2.3 Furnace and Directional Solidification

The Bridgman technique is used to directionally solidify the binary alloys; figure 8 shows the furnace assembly. The furnace assembly is made up of a graphite susceptor kept within an insulating alumina tube to create an approximately 20 cm long, 2.5 cm ID, hot-zone by coupling the susceptor to a 60-watt RF induction power source. About 1.2 cm thick refractory disk kept at the bottom of the hot-zone works as the adiabatic zone; a 0.5 cm long insulating shell is placed at the top of the susceptor to reduce the heat loss there. The entire assembly is kept within a cylindrical, double walled water-cooled quartz enclosure held vertically by the help of stainless steel flanges on its both ends. Graphite crucible, held by a stainless-steel translation rod entering from the bottom flange, can be withdrawn from the hot zone at growth speeds varying from 2 to 90 $\mu m\ s^{-1}$. An approximately 10^{-4} torr dynamic vacuum was maintained within the quartz enclosure during these experiments

Figure 8: Bridgman furnace assembly used for directional solidification experiments

For each experiment, a <100> oriented seed crystal of the same alloy aligned with the growth direction is inserted at the bottom of the crucible; the precast sample alloy is then placed on top of the seed. The cast feed is heated and melted by the furnace; the melt flows down and fuses with the seed crystal below. Care is taken into account to partially remelt the seed. A DC motor coupled with a gear is used to withdraw the crucible from the hot-zone. As it exits the furnace, it is cooled down by radiation to the environment and creates the longitudinal thermal gradient.

2.4 Specimen Preparation and Metallography

Once the crucibles are cooled down they are removed from the furnace, and cut open to take the solidified alloy out. Depending upon the alloy under the experiment, and the obtained mushy-zone length during solidification (calculated from recorded temperature data) several transverse cuts along the samples are made. The distance between each cut is determined based on the proximity to the section-change location, and on the local mushy-zone length. In some cases, if further analysis was of interest, longitudinal cuts were also made through some specimens.

Al-19Cu and Al-7Si specimens were mounted using a thermosetting dry granular epoxy. A heated hydraulic mounting press was used to cure the resin under the pressure of about 20 MPa and temperature of about 120 °C. Each specimen is mounted such that the hot side of the cut sample is available for polishing and imaging. The mounted specimens are ready for grinding and polishing using wetted abrasive grinder. For Al-19Cu and Al-7Si similar polishing procedure is used. Table II shows the detailed steps of this procedure. After each step of grinding/polishing, pads and specimens should be thoroughly cleaned using running water. As it is seen in Table II the last step involves using a 0.05 μm particle size of colloidal silica solution as the polishing agent; if more cleaning is required after this step ultrasonic bath is used to clean the specimen further. The polishing procedure is not very definite, and the most important point during the polishing is to watch the result of each step to see whether the entire surface has been polished evenly and has the same quality throughout. If it is needed the previous step should be repeated. Overpolishing, especially in the last step, may result in microstructures where the softer phase is carved more which creates thick edges between

the harder and softer phases when seen under the microscope; this could introduce dramatic errors in the image analysis.

Table II: Grinding and Polishing Procedure for Al-7Si and Al-19Cu Alloys

Abrasive Grade (grit)	Applied force/specimen (lb)	Time (min)	Polishing Pad rpm	Running Water	Comments
400	3-4	1-1.5	110-130	Yes	
600	3-4	1-1.5	110-130	Yes	
800	3-4	2	110-130	Yes	
1200	3-4	2	110-130	Yes	
PSA polishing pad from HUDSON	4-5	4	110	No	Wet the polishing pad beforehand, and use 3 μm diamond suspension
PSA polishing pad from HUDSON	4-5	4	110	No	Wet the polishing pad beforehand, and use 1 μm diamond suspension
Chemomet I from BUEHLER	5	5	110-130	No	Wet the polishing pad beforehand, and use 0.05 μm Colloidal Silica

2.5 Microscopy, Imaging and Montaging

A 5-megapixel digital camera attached to a metallurgical brightfield inverted Nikon microscope together with SPOT 5.0 software were used to digitally record the alloys microstructures. 50X magnification is usually used for this purpose, and to cover the entire specimen surface with this field of view more than 130 tile images should be taken. Each tile image should have at least 10 to 15 percent of its dimension (height or width) as overlap with its neighbors, so that during the next montaging step of the entire cross-section each individual image in the tile could be located with respect to its neighboring images. There is not a fixed setting to use for imaging in SPOT; light exposure, gamma correction, gain and color filters are determined based on the alloy and the quality of the polish, and might be different for each case. The ideal image quality is when there is distinct light intensity between α-phase and eutectic, constant light intensity across the whole field of view and constant light intensity within one phase (primarily α-phase).

In order to stich the tile images and to get the final microstructure of the transversely cut specimen, Interactive Layout option of Photomerge tool of Adobe Photoshop CS.5.1 was used. Overlapping images are automatically overlaid by the software using methods to first identify the location of each tile, then calibrating optical aberrations and finally blending images, if required. The most problematic issues for the stitching step are having non-uniform intensity within each image and having out of focus images among the batch which is being overlaid.

2.6 Image Analysis

From the montaged microstructures following three types of data are extracted; fraction eutectic, primary dendrites trunk diameter, and primary dendrite nearest neighbor spacing. Fraction eutectic is simply calculated by division of the area occupied by eutectic phase by the total cross-sectional area of the specimen. Separating these two regions, however, is not very simple. Eutectic phase itself consists of two phases, α and β. The α within the eutectic is the same as the α primary dendrite, and is often interconnected to the primary α phase. Therefore, their light absorption and color contrast are identical. This requires special image analysis techniques and procedures to be developed. Specialized procedures designed for ImageJ (a free open-source image processing software) are presented in detail in section 2.10.5 of ref. [38]. There is an error of about 2% involved in the fraction eutectic measurements rooted in the particle size cut-off values which is reflected in all the plots corresponding to composition in the result section. It is recommended that the procedure to be read from the ref. [38] to get the method used for this purpose.

Primary dendrites trunk diameters are measured by drawing two nearly diagonal lines, each one is the minimum distance spanning the trunk. If the dendrite's <100> orientation is perfectly aligned with the direction of solidification, then on a transverse microstructure these two lines would be perpendicular to each other. First step of this measurement is to activate the appropriate measurements option from the Analyze → Set Measurements → Bounding Rectangle menu in ImageJ; then by choosing the line-selection tool and drawing a line as trunk diameter, measurement could be performed from Analyze→ Measure menu (or simply by pushing "m" on keyboard). Serious care

should be taken to not miss any drawing without measuring it, because each pair of consecutive measurements represents one trunk and if one measurement is accidentally missed then the first measurement of the next pair gets considered as part of the pair for the previous measurement, which creates a large error in the next calculations. After the measurements for all the trunks are done the "Result" window should be saved. ImageJ saves the contents of the result window as .csv file which could be opened by Microsoft Excel. But, since this type of file is not readable by MATLAB, which is used to process the raw measurements, it should be saved again as .xlsx to be used later. A MATLAB code was developed which gets this .xlsx file as the input and calculates each dendrites trunk diameter, each dendrite nearest neighbor spacing, average of trunk diameters and average of nearest neighbor spacings within the cross-section and some more features, and outputs the result as another .xlsx file. This code is presented in the Appendix.

Chapter III

Results and Discussion

3.1. Directional solidification of Al-7Si and Al-19 Cu with uniform sample cross-section

3.1.1. Effect of Alloy Composition and Growth Speed on Microstructure

After careful preparation of specimens' surfaces and recording the microstructures, they could be studied in terms of how growth speed and thermophysical properties of the alloy influence the microstructure. Figures 9(a) and 9(b) show the microstructures of Al-19Cu solidified at 10 and 29.1 μm/s, respectively; while figs. 9(c) and 9(d) correspond to Al-7Si grown at 10 and 29.1 μm/s, respectively. The first thing to notice is the inhomogeneity in the distribution of the primary α-phase within the cross-section especially in the slower growth speeds specimens (figs. 9(a) and 9(c)). As it can be seen, primary dendrites are clustered in one region, usually in the center, while the opposite region or sample periphery is mostly of eutectic microconstituent. This is much

more evident in Al-19Cu as compared to the Al-7Si, especially at low growth speed. The other noticeable fact is long secondary arms extending towards the regions with higher eutectic structure, while the secondaries in the interior of the specimens are much shorter.

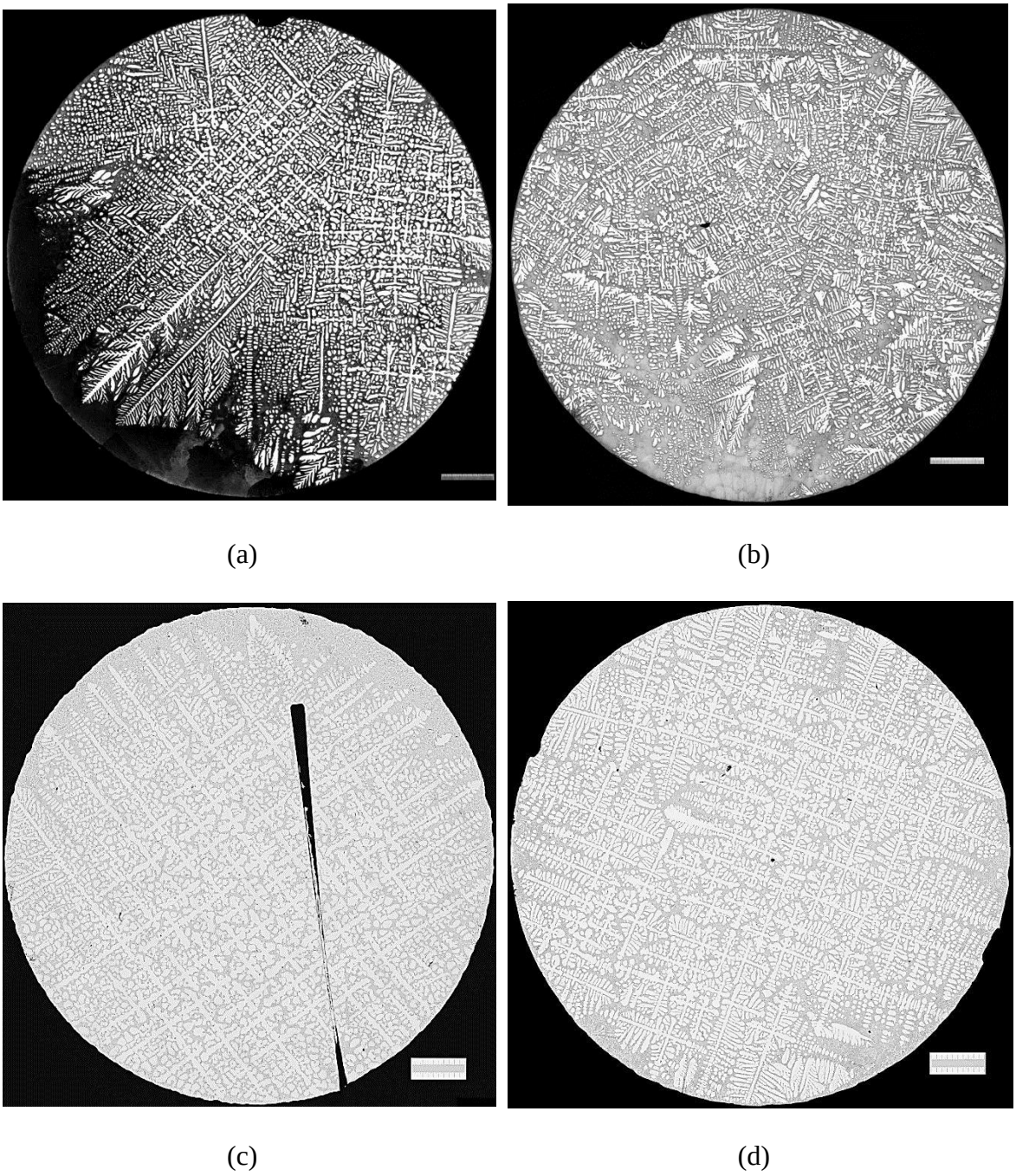

(a) (b)

(c) (d)

Figure 9: Transverse microstructures of directionally solidified alloys in constant cross-section mold. (a) and (b) are Al-19Cu solidified at 10 µm/s, 81 K/cm and 29.1 µm/s, 48 K/cm, respectively; (c) and (d) are for Al-7Si grown at 10 µm/s,40 K/cm and 29.1 µm/s 51 K/cm, respectively.

3.1.2. Effect of Alloy Composition and Growth Speed on Radial Macrosegregation

As discussed in the introduction, any radial thermal gradient provides the necessary condition for the thermosolutal convection to begin and mushy-zone to become steepled. This thermosolutal convection advects the solute towards the mold walls accumulating it there and postponing the solidification in those regions to lower temperatures. Secondary arms in the interior do not have space to grow over distances beyond the primary arm spacing, but those on the periphery of the steepled (convex) mushy-zone find more space to grow sideways and thus become longer.

Since the central region of the clustered dendritic microstructures on transverse view are formed first during solidification, and regions around are gradually solidified as steepled mushy-zone traverses upwards, the radial macrosegregation on a transverse cross-section of the directionally solidified sample could be quantified by measuring the fraction eutectic, f_E, while moving radially from the center of mass of the primary α-phase towards the periphery of the specimen. To this end, an image processing technique was designed such that the fraction eutectic within concentric rings, centered at the center of mass of primary dendrites, are measured and they are assumed to correspond to the radial area fraction solidified till each particular ring. For example, f_E measured from the innermost circle corresponds to the "area of the inner most circle / total area of the specimen cross-section", and that measured from the first ring corresponds to "(area of the inner most + area of the first ring) / total area of the specimen cross-section)", and so on. This method is explained in more details in the section 2.3 of ref. [39]. Figure 10

shows a typical microstructure where the concentric red-colored rings are overlaid on the image and primary dendrites are colored while the eutectic phase is seen as gray.

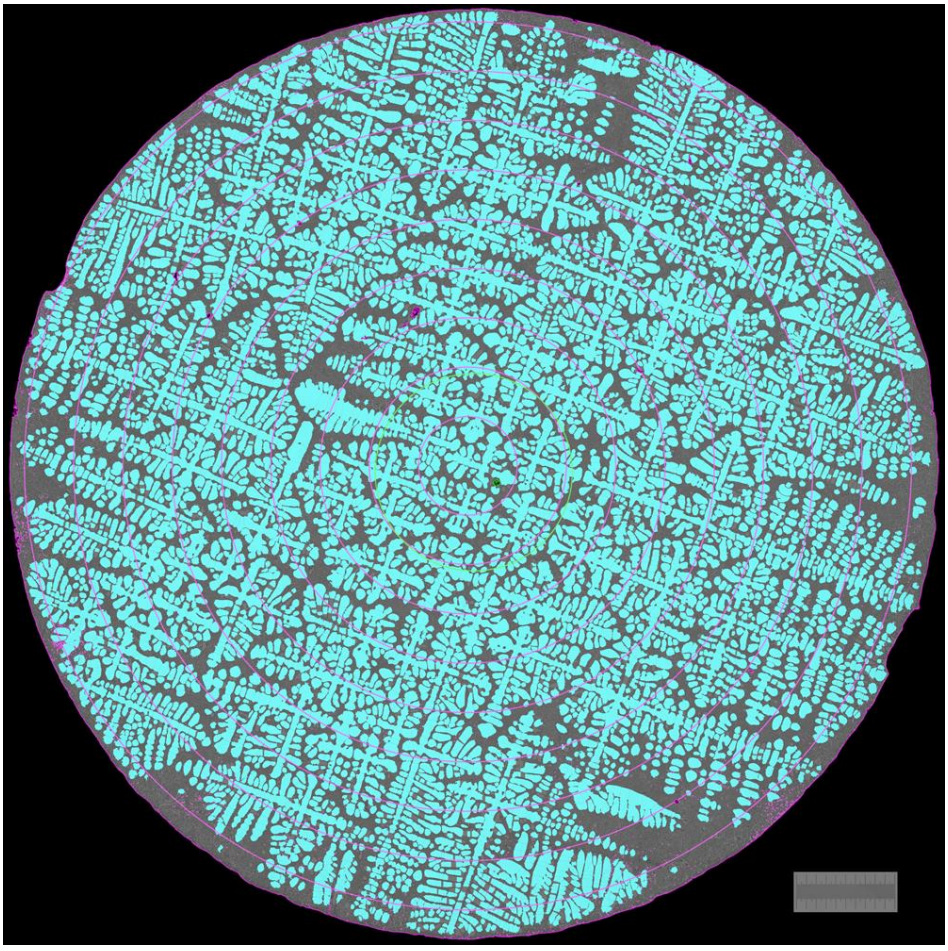

Figure 10: Typical transverse microstructure of directionally solidified Al-7Si alloy with concentric ring overlay for analysis of radiaal macrosegregation.

By knowing the fraction eutectic within each ring (or the entire cross-section) the local solute concentration is calculated by using equations below.

For hypoeutectic Al-Si alloys:

$$C_{0_{Si}} = 11.60 f_E + 1.094 \qquad (8)$$

and for hypoeutectic Al-Cu alloys:

$$C_{0_{Cu}} = 28.86 f_E + 4.408 \quad (9)$$

At the nominal concentration of the alloys used in this research, the maximum error for the equation (8) is ± 0.28 wt.% Si, and for equation (9) is ± 0.38 wt.% Cu. Appendix of reference [39] explains the approach used to derive the equations above.

As a part of a large scope, the temperature data collected during our experiments were used as the boundary conditions to simulate the solidification and fluid flow effects on the macrosegregation at The University of Arizona. In the sections below, our macrosegregation measurements will be presented; and results from the numerical simulation will be used where they are helpful to elucidate the experimental observations. Appendix B explains some main features of the simulations conducted in the university of Arizona.

Using the method mentioned above (and explained in the Appendix of ref. [39]), radial macrosegregation was quantified on transverse sections away from the cross-section change, both before contraction and after expansion. Each of the figures 11(a) and 11(b) show two radial macrosegregation on Al-19Cu samples grown at 10 and 29.1 μm/s; while figs. 11(c) and 11(d) correspond to Al-7Si grown at 10 and 29.1 μm/s, respectively. The ordinates are solute concentration in weight percent, and abscissas are radial area fraction solidified. Circles and squares are results from image analysis of samples, and dashed and dotted curves are data extracted from the numerical simulation results.

As it is seen in all of the subfigures, there are radial macrosegregations such that the central regions of the dendrites cluster, corresponding to the low area fraction solidified, are solute depleted and there is a gradual increase towards the samples

peripheries at high area fraction solidified. It should be pointed out that the overall concentration within each cross-section, which is the same as area-based integration of the values seen in figs. 11(a)-11(d), is the initial alloy concentration C_0.

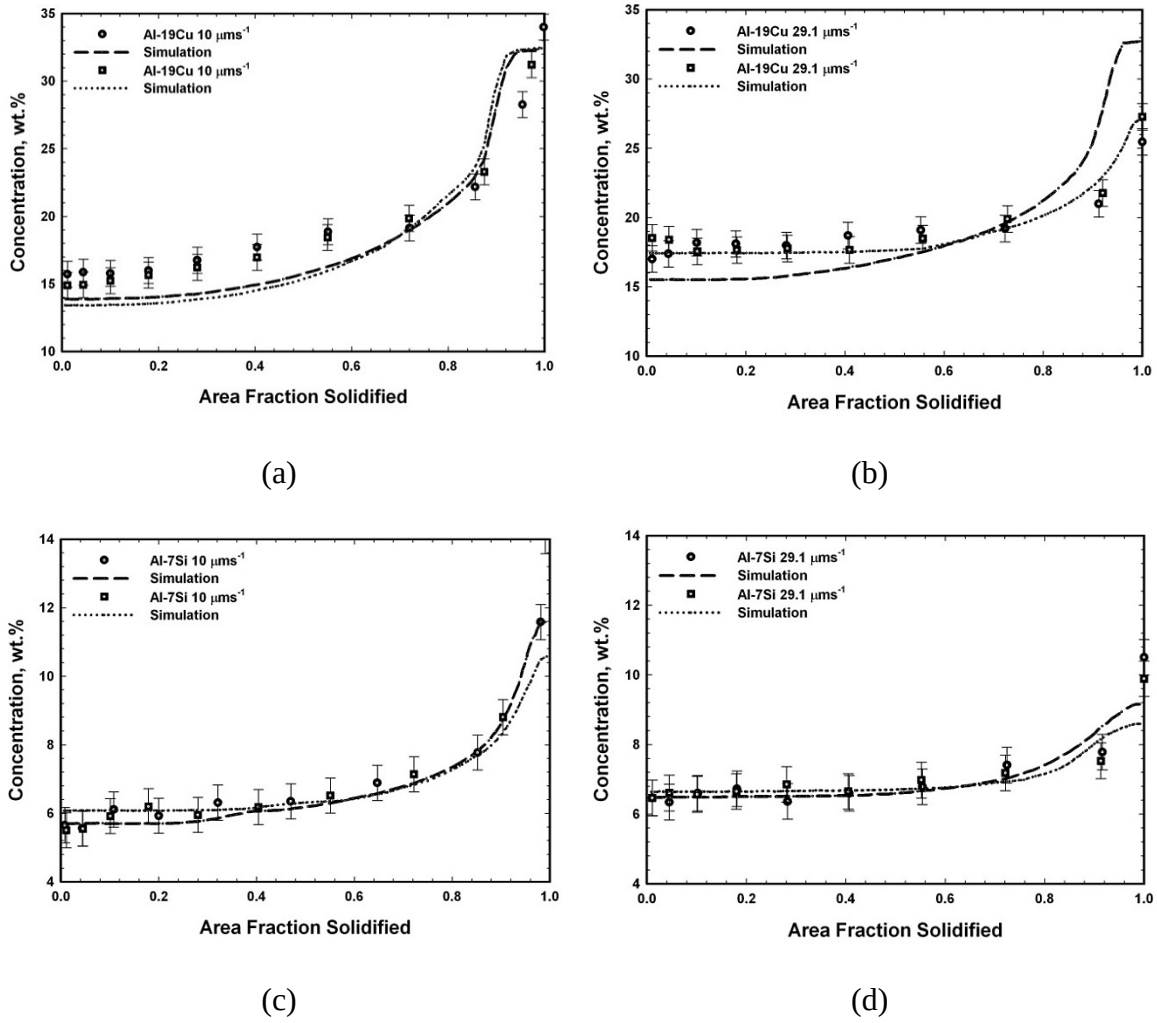

Figure 11: Experimentally measured and simulation results of radial macrosegregation away fron cross-section change in directionally solidified alloys. (a)Al–19Cu alloy solidified at10 μm/s; (b)Al–19Cu alloy solidified at 29.1 μm/s; (c)Al–7Si alloy solidified at10 μm/s; (d)Al–7Si alloy solidified at 29 μm/s

Here the effect of growth speed on radial macrosegregation could be studied by comparing figure 11(a) versus 11(b), or 11(c) versus 11(d). Looking at the experimental data plotted in figure 11(a) and 11(b), it is evident that at low area fraction solidified which corresponds to the central portion of the primary dendrite cluster (i.e. the leading

end of the dendrite array) the copper concentration is about 15 wt. %, and then it increases as one moves towards the higher fraction solidified (i.e. the outer regions on the transverse sections or the lagging dendrites array tips) to about 34 wt. %. Similar behavior is seen in figure 11(b), grown at faster speed, but at low fraction solidified, copper concentration is around 17-18 wt. %, remains almost the same up to 0.3 fraction area solidified, and then takes off to its maximum of about 26 wt. % at the periphery. This means that there is stronger radial macrosegregation at slower grown samples. Similar behavior is seen by comparison of figures 11(c) and 11(d). Also, at faster growth speed, fig. 11(b), the concentration remains constant up to an area fraction solidified of about 0.3 while at slower growth speed, fig. 11(a), the increase starts from lower fraction solidified values. These two observations are attributed to the degree of steepling. At faster growth speed, the mushy zone-liquid interface is flatter at the central region and becomes curved (steepled) midway through the periphery; but at slower growth speed, especially in the case of Al-19Cu, almost the entire interface is curved and has a dome-like convex geometry. This results in radial macrosegregation profiles similar to those shown in figures 11(a) and 11(b) (or 11(c) and 11(d)).

The degree of macrosegregation, which is an indication of the degree of steepling, is obviously lesser in Al-7Si than in Al-19Cu grown at similar speeds (compare fig. 11(a) with 11(c) or fig. 11(c) with 11(d)). One order of magnitude larger solutal expansion coefficient, β_C, in Al-19Cu increases the solute-rich liquid's density much more effectively; this results in a stronger thermosolutal convection advecting solute outwards to the mold's wall. Consequently, mushy-zone becomes more steepled and more solute accumulates around the periphery increasing the radial macrosegregation. The Al-7Si

sample grown at 29.1 μm/s (fig. 11(d)) shows the least radial macrosegregation among all; the silicon concentration profile remains flat up to about 0.5 area fraction solidified and then increases to its maximum at the mold wall, indicative of weakest thermosolutal convection and flattest (least steepled) mushy zone-liquid interface.

The simulation results are in good agreement with the experimentally measured data except in one case of Al-19Cu grown at 29.1 μm/s (fig. 11(b)). This sample, especially in the location corresponding to the specimen which was analyzed for its radial macrosegregation, had several grains, and the <100> orientation of some of them were not aligned with the growth direction. The model used for the simulations assumes that the dendrites are parallel to the growth direction, so the permeability tensor included in the model has one component parallel and one component perpendicular to the dendrites. It is believed that the discrepancy between the actual data and predictions from the simulation may be because of this assumption.

It should be mentioned that, in these two alloy systems, the solute advection happens radially outwards, resulting in radial macrosegregation as discussed earlier, but since the liquid phase is either stable (in Al-19Cu) or almost neutral (in Al-7Si) with respect to buoyant forces, there is no longitudinal solute movement and mixing with the bulk liquid ahead of the solidifying mushy-zone. Hence, no macrosegregation occurs along the length of these directionally solidified samples [23].

3.2. Directional solidification of Al-7Si and Al-19 Cu through an abrupt Cross-Section Decrease

3.2.1. Effect of Cross-Section decrease on the Dendritic Microstructures

Transverse microstructures of both Al-19Cu and Al-7Si, grown at different speeds, in the vicinity of the cross-section decrease are shown in figs. 12(a)-12(d).In each figure the lower part shows the section before the contraction, and the upper part is for the smaller cross-section after the contraction. Distances from cross-section change are shown in the figure caption.

Microstructures in the lower part of figs. 12(a) and 12(b) show heavily clustered dendrites, much more so in the slower grown sample in fig. 12(a), while there are regions around the periphery with pure eutectic microconstituent; this is indicative of strong thermosolutal flow and steepled mushy-zone. The narrow portion of the mold is right at the center of the larger diameter below; therefore, the core of the mushy-zone enters into the contraction. The upper part of fig. 12(a) belong to 2 mm after section-decrease; and although the center of mushy-zone has entered into the smaller diameter portion, it appears that steepling has already been established at this location (lower-left of the microstructure is eutectic-rich). The microstructure shown in the upper part of fig. 12(b) is almost uniform with very slight indication of steepling.

Both lower parts of figs. 12(c) and 12(d) show dendrites clustering, but it is more evident in the slower grown sample. Microstructures of Al-7Si samples near the contraction in the smaller diameter portion do not show obvious dendrite clustering (upper parts of figs. 12(c) and 12(d)).

The other noticeable observation in all the cases seen in figs. 12(a)-12(d) is that the dendritic arrays maintain their orientation as they grow into the narrow section neck; both Al-7Si samples appear to be single crystal before and after the contraction, and grains in the central part of the Al-19Cu samples grow into the smaller cross-section above while maintaining their orientation.

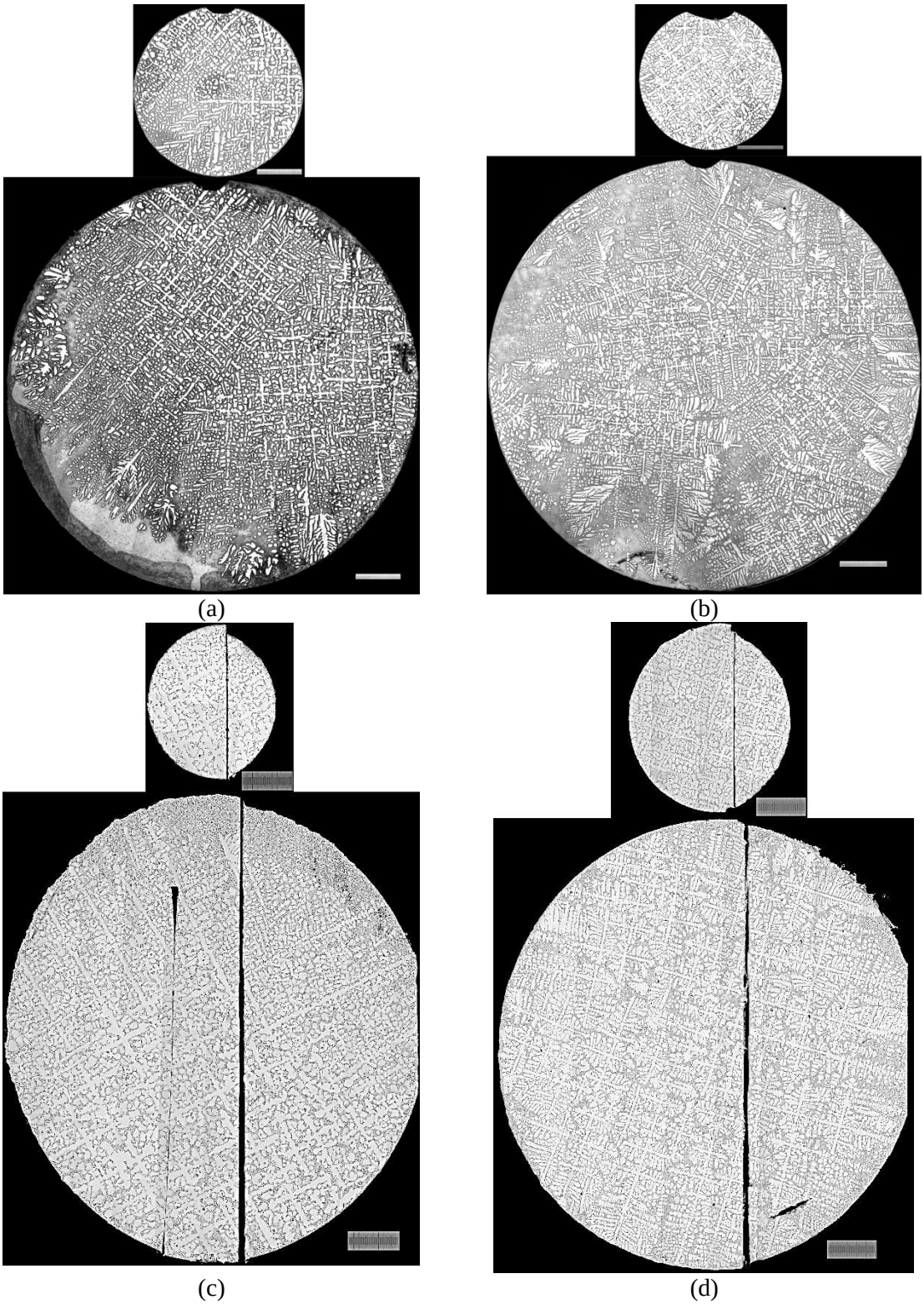

Figure 12:Transverse microstructures of directionally solidified Al-19Cu and Al-7Si through a cross-section decrease: (a) Al-19Cu solidified at 81 K cm^{-1}, 10 μm s^{-1}; distances of specimens fromsection change are −0.9 and +2 mm, respectively; (b) Al-19Cu solidified at 48 K cm^{-1}, 29.1 μm s^{-1}; distances of specimens from section change are −3.6 and +1.9 mm, respectively; (c) Al-7Si solidified at 33 K cm^{-1}, 10 μm s^{-1}; distances of specimens fromsection change are −3 and +0.7 mm, respectively; (d) Al-7Si solidified at 51 K cm^{-1}, 29.1 μm s^{-1}; distances of specimens from section change are −1.2 and +2.5 mm, respectively; Scales are 1 mm.

3.2.2. Effect of Abrupt Area Decrease on Macrosegregation

As discussed earlier, during solidification there always exists a fluid flow due to the shrinkage resulting from liquid to solid phase transformation. When the mushy-zone is away from the cross-section change a constant downwards shrinkage flow, proportional to growth speed, is feeding the solidification shrinkage; as it approaches the contraction, the melt from narrow section above has to feed the shrinkage happening in the larger diameter section below. Therefore, the shrinkage flow intensity increases. We will call this flow as *cross-section-change-induced-shrinkage-flow*. The interaction between the "steepling" type thermosolutal convection and shrinkage flow in the vicinity of the area contraction will be expected to influence the local longitudinal and the radial macrosegregation.

3.2.2.1. Longitudinal Macrosegregation

In order to determine the longitudinal macrosegregation, transverse microstructures of both alloys at several sections along the sample length, both, before and after contraction were examined. Fraction eutectics were measured by the method explained earlier and average solute concentrations for each cross-section were calculated using equations (8) or (9). The data from the simulations carried out at The University of Arizona were also analyzed to elucidate the flow effects in this region. At each longitudinal distance, the concentration data from the simulations were averaged on an area-based fashion and plotted in figures 13(a)-13(d). Figures 13(a) and 13(b) show the average concentration of solute along the Al-19Cu samples grown at 10 and 29.1 μm/s, respectively; 13(c) and 13(d) are for Al-7Si grown at 10 and 29.1 μm/s, respectively.

Ordinates are the solute concentration and abscissas are distances from the cross-section contraction; zero corresponds to the section-change location.

In all the cases, the mean solute content at locations away from the contraction neck is the nominal alloy concentration; but a sudden positive macrosegregation right before section-decrease followed by a negative macrosegregation immediately after it is seen. As the mushy-zone approaches the contraction, the solute at the array tips immediately ahead of the mushy-zone's front gets entrapped on the top-shelf and accumulated there causing a solute built-up. At the same time shrinkage flow, bringing in liquid with C_0 concentration from the smaller cross-section, is intensified because it is feeding the solidification shrinkage still happening at the larger cross-section below. This together with the fact that the central regions of the steepled mushy-zones—which are the regions that enter the contraction—are already solute depleted due to the "steepling" thermosolutal convection discussed before, cause the sharp decrease right after the cross-section decrease. The concentration then gradually increases to its steady-state nominal values. The magnitude of the solute built-up before the contraction is more at slower grown samples in both alloys (fig. 13(a) vs. 13(b) and 13(c) vs. 13(d)); this is because first the extent of steepling decreases with increasing growth speed, and second, stronger shrinkage flow at faster growth speed tends to decrease the degree of steepling more as compared to what it does at slow growth speed.

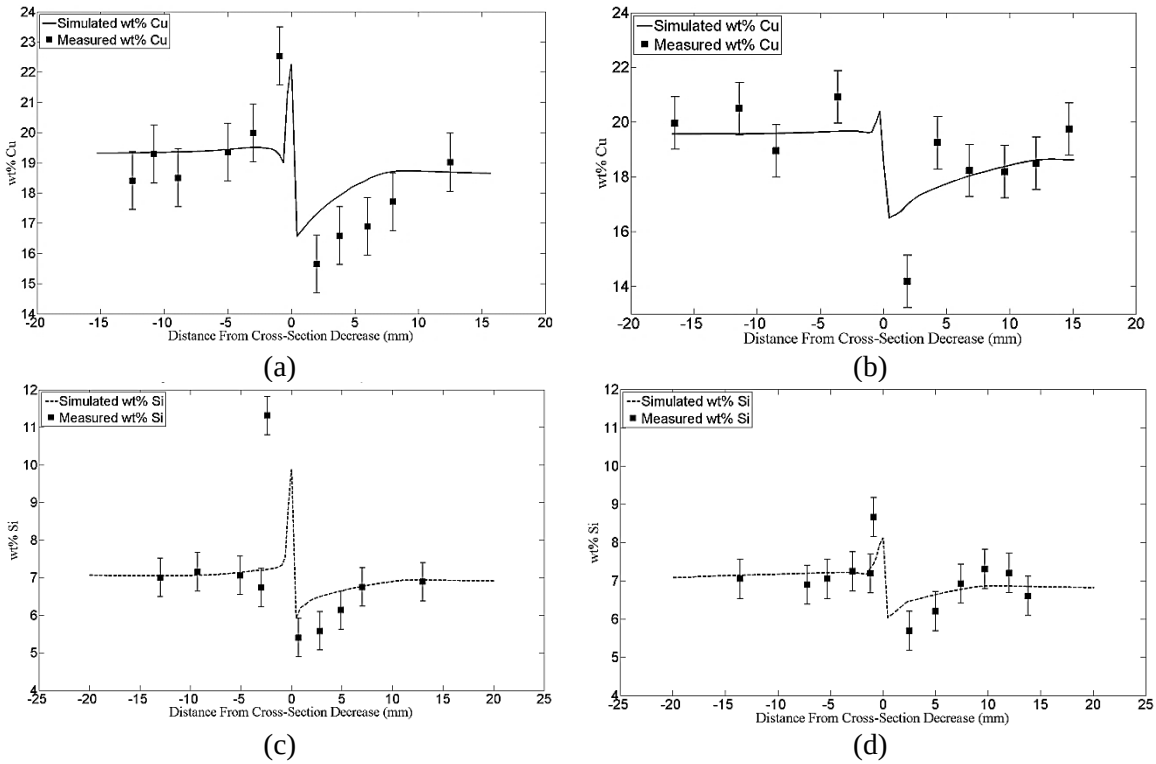

Figure 13: Longitudinal concentration distribution of directionally solidified Al-19Cu and Al-7Si close to cross-section decrease: (a) Al-19Cu solidified at 81 K cm−1, 10 μms−1; (b) Al-19Cu solidified at 48 K cm−1, 29.1 μm s−1; (c) Al-7Si solidified at 33 K cm^{-1}, 10 μm s^{-1}; (d) Al-7Si solidified at 51 K cm^{-1}, 29.1 μm s^{-1}.

3.2.2.2. Radial Macrosegregation

3.2.2.2.1. Radial Macrosegregation in the Larger Diameter Section before Contraction

The same method explained in the section 3.1.2 was used to measure the radial macrosegregation on cross-sections close to the contraction, both before and after section-change. Figures 14(a)-14(d) show radial macrosegregation profiles of specimens near cross-section decrease in the larger diameter portion of samples. The distances of specimens from section-change are in the figures' legends; negative distance indicates transverse sections before section decrease. Figures 14(a) and 14(b) are for Al-19Cu, and 14(c) and 14(d) are for Al-7Si grown at 10 and 29.1 μm/s, respectively. The ordinates in these plots are the ratio of the concentration of solute within the ring to the overall cross-section concentration, and abscissas are area fraction solidified.

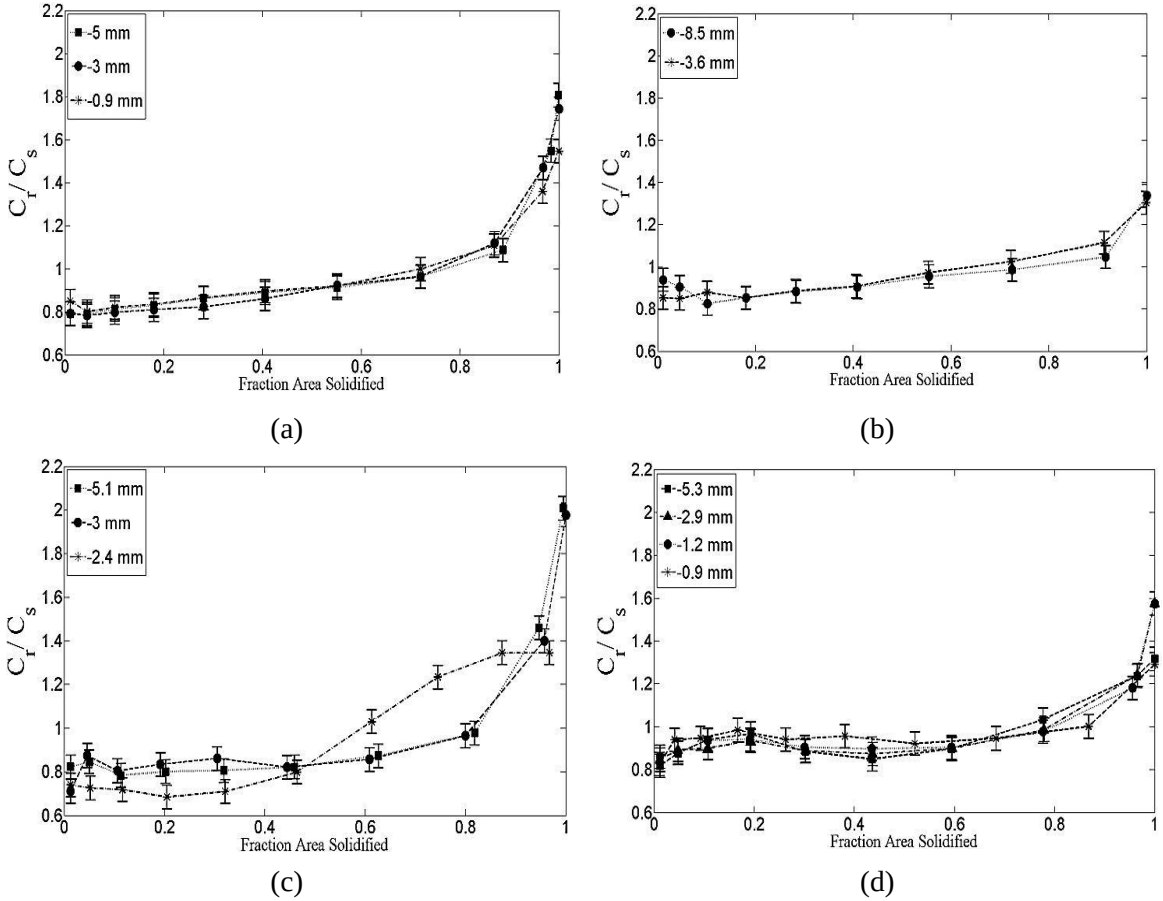

Figure 14: Experimental results of radial macrosegregation of Al-19Cu and Al-7Si directionally solidified into a contraction. All the figures belong to the larger sections before contraction.: (a) and (b) correspond to Al-19Cu grown at 10 μm s−1 and 29.1 μm s−1, respectively; (c) and (d) correspond to Al-7Si grown at 10 μm s^{-1} and 29.1 μm s^{-1}, respectively. Fraction area solidified is calculated from center of mass of the steepled dendritic array.

It was shown in the section 3.1.2 that the slower the growth speed the more steepled the mushy-zone and the stronger the thermosolutal (steepling) convection. Also, it was discussed that greater solutal expansion coefficient in Al-19Cu creates stronger thermosolutal convection as compared to that in Al-7Si. Hence, Al-19Cu grown at 10 μm/s has the most and Al-7Si grown at 29.1 μm/s has the least steepled mushy-zone.

Three available Al-19Cu specimens close to the contraction, grown at 10 μm/s were analyzed for the radial macrosegregation and the results are seen in figure 14(a). There are obvious radial macrosegregation; solute depleted regions in the center (low fraction solidified) and gradual increase towards the samples periphery; the profiles are

very similar in all the cases. The closest section to the contraction in the Al-19Cu sample grown at 29.1 μm/s was at -3.6 mm (fig. 14(b)). The profiles in this case are very similar to those seen in the sample grown at 10 μm/s with less macrosegregation, as expected at faster growth speed.

The closest section to contraction available in Al-7Si grown at 10 μm/s (at -2.4 mm) shows different radial macrosegregation profile (see fig. 14(c)); this behavior is very similar to those seen in fig. 14(d) for the same alloy grown at 29.1 μm/s. When the steepled mushy-zone gets closer to the contraction neck, the shrinkage flow, anti-parallel to the growth direction, is intensified and brings in the liquid with the original bulk concentration, C_0, into the solidifying region. The liquid right on top of the mushy-zone is already segregated; in the interior, it has less concentration than C_0 and close to the mold walls is the place where solute has been accumulated due to the thermosolutal convection. C_0 liquid brought in the region locally increases the concentration at the center and changes the radial macrosegregation pattern there. The strength of this cross-section-change-induced-shrinkage-flow determines how deep this flow can influence the mushy-zone and thus the resulting macrosegregation. We know that the shrinkage flow is about 3-times stronger at 29.1 μm/s than in 10 μm/s. For Al-7Si grown at 29.1 μm/s even at -5.3 mm before the contraction, this effect is visible (fig. 14(d)), but for that grown at 10 μm/s the effect is only seen at -2.4 mm and locations further away from the section change (-3 and -5.3 mm) show the usual radial macrosegregation profile seen earlier. The extent of radial macrosegregation, however, is greater in the slower grown sample as compared to the faster one (fig. 14(c) vs. 14(d))

Since the thermosolutal convection is stronger and more dominant in Al-19Cu samples, the shrinkage flow effect is not as influential as it is in Al-7Si. Therefore, the radial steepling driven macrosegregation pattern is less affected in Al-19Cu than in Al-7Si.

3.2.2.2.2. Radial Macrosegregation in the Smaller Diameter Section after Contraction

Radial macrosegregations on several specimens from the smaller diameter portions after the contraction are plotted in figures 15(a)-15(d). Figures 15(a) and 15(b) are for Al-19Cu grown at 10 and 29.1 μm/s, respectively; and 15(c) and 15(d) are for Al-7Si grown at 10 and 29.1 μm/s, respectively. Ordinates and abscissas are similar to those in figure 14. In general, the extent of the radial macrosegregation is much less in the smaller diameter as compared to those before the section-decrease, regardless of the alloy and growth speed. In all the cases, the macrosegregation profile remains flat up to about fraction area solidified of 0.9 and then some solute accumulation is seen near the periphery of samples; this increase in solute content, however, is greater in the slower growth speed in both alloys (fig. 15(a) vs. 15(b) and 15(c) vs. 15(d)). Comparison of radial macrosegregation in different alloys grown at the same speed in the narrow portion of the mold is not showing much difference (fig. 15(a) vs. 15(c) and 15(b) vs. 15(d)), which implies that the mold diameter is an important factor in the resulting degree of steepling and macrosegregation during directional solidification.

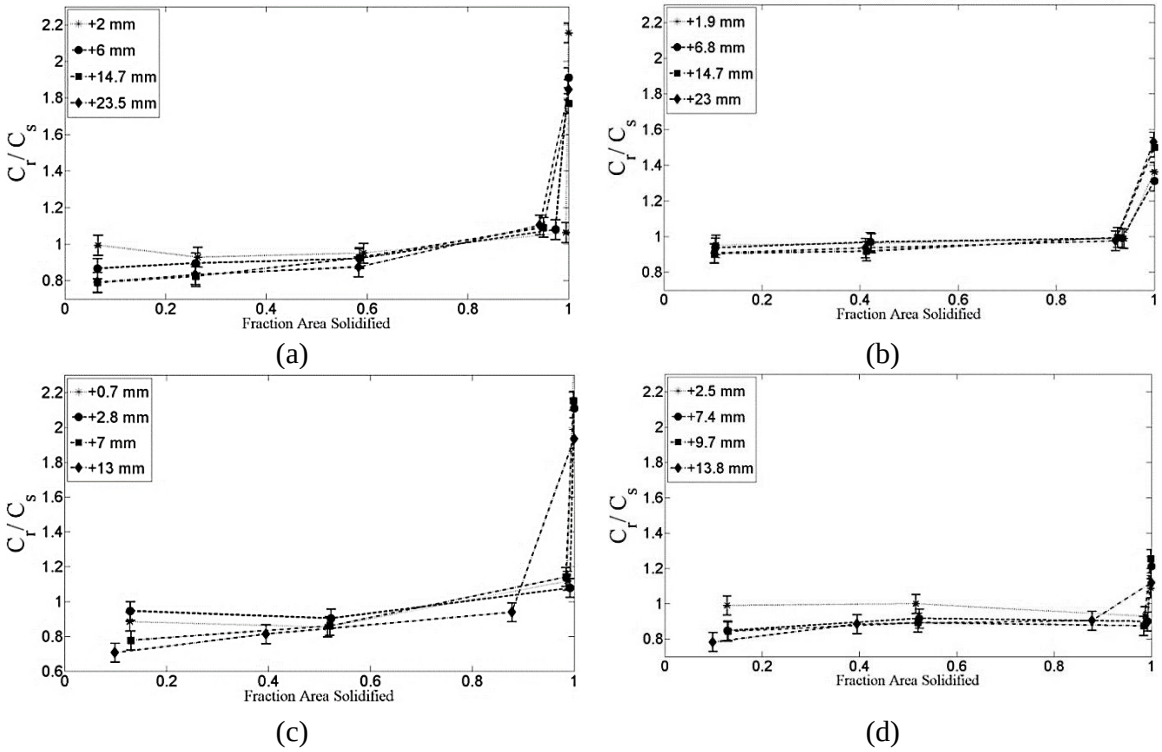

Figure 15: Experimental results of radial macrosegregation of Al-19Cu and Al-7Si directionally solidified into a contraction. All the figures belong to the smaller sections after contraction.: (a) and (b) correspond to Al-19Cu grown at 10 μm s^{-1} and 29.1 μm s^{-1}, respectively; (c) and (d) correspond to Al-7Si grown at 10 μm s^{-1} and 29.1 μm s^{-1}, respectively.

3.3. Directional solidification of Al-7Si and Al-19 Cu through an abrupt Cross-Section Increase

3.3.1. Influence of Cross-section Expansion on Dendritic Microstructure

Transverse microstructures of both alloys, grown either at 10 or 29.1 μm/s, near the expansion, before and after it, were metallographically prepared and digitally recorded in the same manner explained before. Figures 16(a)-16(d) show these microstructures; the bottom part of each figure is from the specimen right before the expansion. The first thing to notice is that in all the cases the microstructures from the smaller diameter portion show dendrite clustering (indicative of mushy-zone steepling) while there was almost no noticeable sign of steepling in the same alloys at the beginning

of the narrow portion (see top part of figs. 12(a)-12(d)). This means that steepling is happening in these two alloys—commensurate with the growth conditions—even within the section with 3.2 mm in diameter, but it takes longer distances for the thermosolutal flow to be established and to influence the mushy zone-liquid interface geometry.

Microstructures from the larger diameter portions after the expansion are shown in the top part of figs. 16(a)-16(d). Dendrites clustering is evident in all of them, much more so in slower grown ones. Long secondary arms extending outwards into the eutectic-rich regions is another indication of thermosolutal convection and steepled mushy-zone very close to the expansion in the larger diameter portion of directionally solidified Al-19Cu and Al-7Si samples.

By comparison of the microstructures of the bottom part of figs. 16(a) and 16(b) with those in the top part of figs. 12(a) and 12(b), respectively, which belong to the same alloy with the same growth condition, it will be seen that as the mushy-zones of Al-19Cu samples traverse into the smaller-diameter section those grains which are not perfectly aligned with the growth and heat extraction direction (seen in the top part of figs. 12(a) and 12(b)) are not surviving all the way to the top of the narrow section and only a single grain, in each case, which is more favorably aligned is growing. Therefore, before the expansion there are only single grains present. In Al-7Si samples there were already single grains growing into the smaller cross-section (see the top part of figs. 12(c) and 12(d)) and they maintained their orientation during the solidification in this section (see the bottom part of figs. 16(c) and 16(d)).

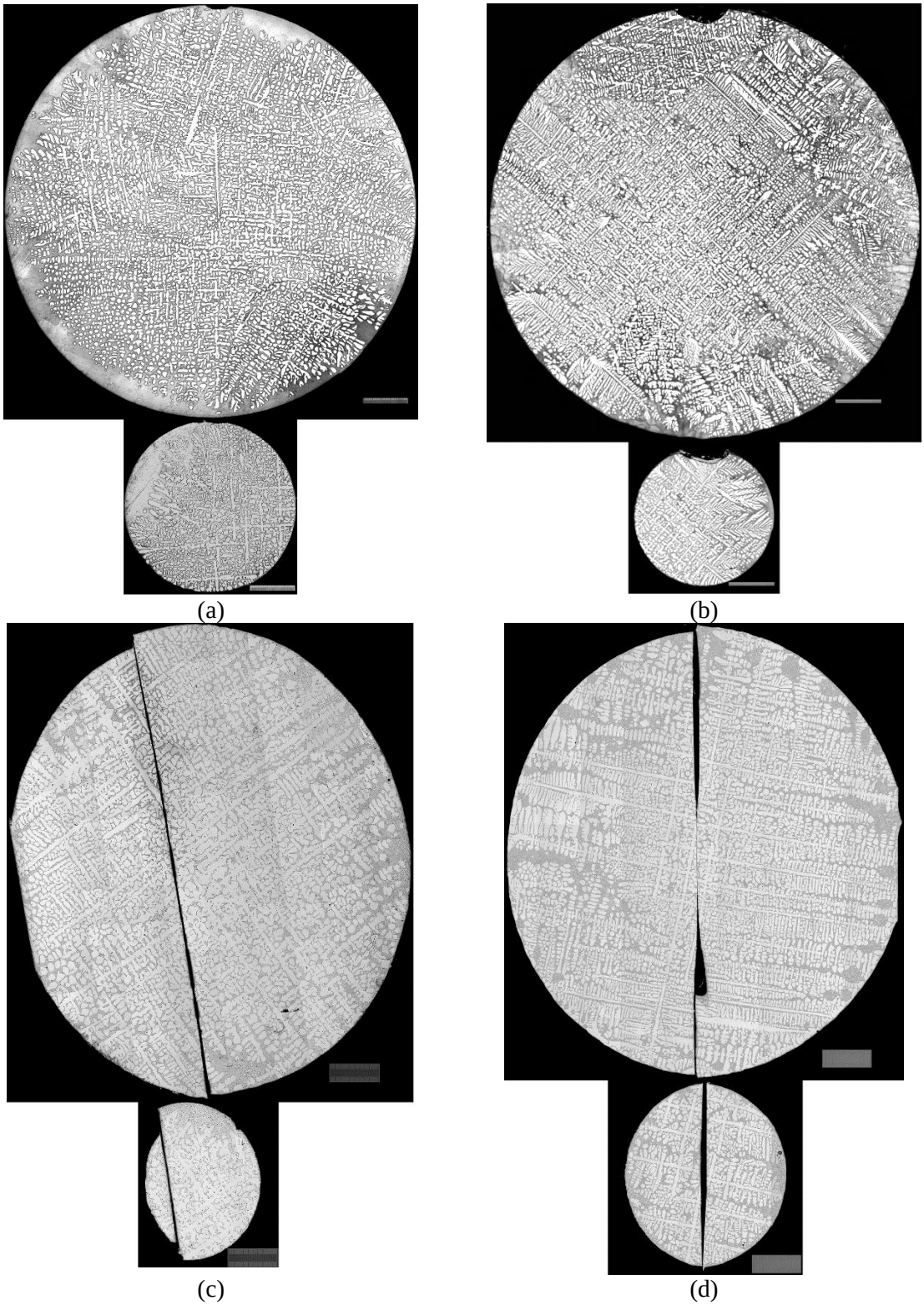

Figure 16: Transverse microstructures of directionally solidified Al-19Cu and Al-7Si through a cross-section increase. (a) Al-19Cu solidified at 92 K cm^{-1}, 10 μm s^{-1}, distance of transverse sections from section-change are -1.8 and +0.3 mm, respectively. (b) Al-19Cu solidified at 53 K cm^{-1}, 29.1 μm s^{-1}, distances of transverse sections from section-change are -0.8 and +1.5 mm, respectively. (c) Al–7Si solidified at 40 K cm^{-1}, 10 μm s^{-1}; distances of microstructures from the section increase are -1.2 and +2.5 mm; (d) Al–7Si solidified at 51 K cm^{-1}, 29.1 μm s^{-1}, distances of microstructures from section increase are -1.6 and +0.7 mm. Scales are 1 millimeter.

3.3.2. Longitudinal Macrosegregation in the Vicinity of Cross-section Expansion

Longitudinal macrosegregation along the length of the samples solidified through an abrupt cross-section increase are show in figures 17(a)-17(d). Symbols in the figures indicate the experimentally measured values and the solid lines are area-based mean solute content extracted from the numerical simulations results. Figures 17(a) and 17(b) are for Al-19Cu, and 17(c) and 17(d) are for Al-7Si grown at 10 and 29.1 μm/s, respectively.

As presented earlier, during directional solidification through expansion the larger cross-section melt above feeds the solidification shrinkage in the smaller diameter portion below. Therefore, the area-induced shrinkage flow is minimal and has limited influence on the solidifying mush below; consequently, average solute content along the sample length remains relatively unaffected by the section-change. Simulations, however, predict a sharp negative macrosegregation right on the shelf just after the expansions. As the front of the mushy zone reaches the expansion, side-arms of the dendrites around the mushy-zone grow and extend side-ways to fill the space of larger diameter portion. At the same time C_0 liquid preexisting on the expansion platform are solidified. As a result of formation of solid α-phase dendrites, solute is rejected into the liquid phase. This solute is getting carried away outwards and upwards by the thermosolutal convection; since the graphite mold below does not allow any flow or diffusion of solute, regions right above the mold shelf remain solute depleted. This is evident in the longitudinal sections shown in Figure 21(a)-21(2) which will be discussed later. Experimental measurements, however, could not be carried out on a transverse section immediately after and very

close to the section increase. Hence, experimental data corresponding to the minimum shown by the simulations in 17(a)-17(d) are not available.

Stronger thermosolutal convection and longer solidification time at slower growth speed allows more of this solute to be swept away, therefore more negative macrosegregation would be expected in those cases (compare figs. 17(a) vs. 17(b) & 17(c) vs. 17(d)). Also, stronger steepling flow in Al-19Cu than in Al-7Si alloys solidified at the same speed leaves the expansion platform with more negative macrosegregation (compare figs. 17(a) vs. 17(c) & 17(b) vs. 17(d)). After this negative macrosegregation, the solute concentration rises until it reaches its steady-state value commensurate with the constant large cross-section portion of the mold.

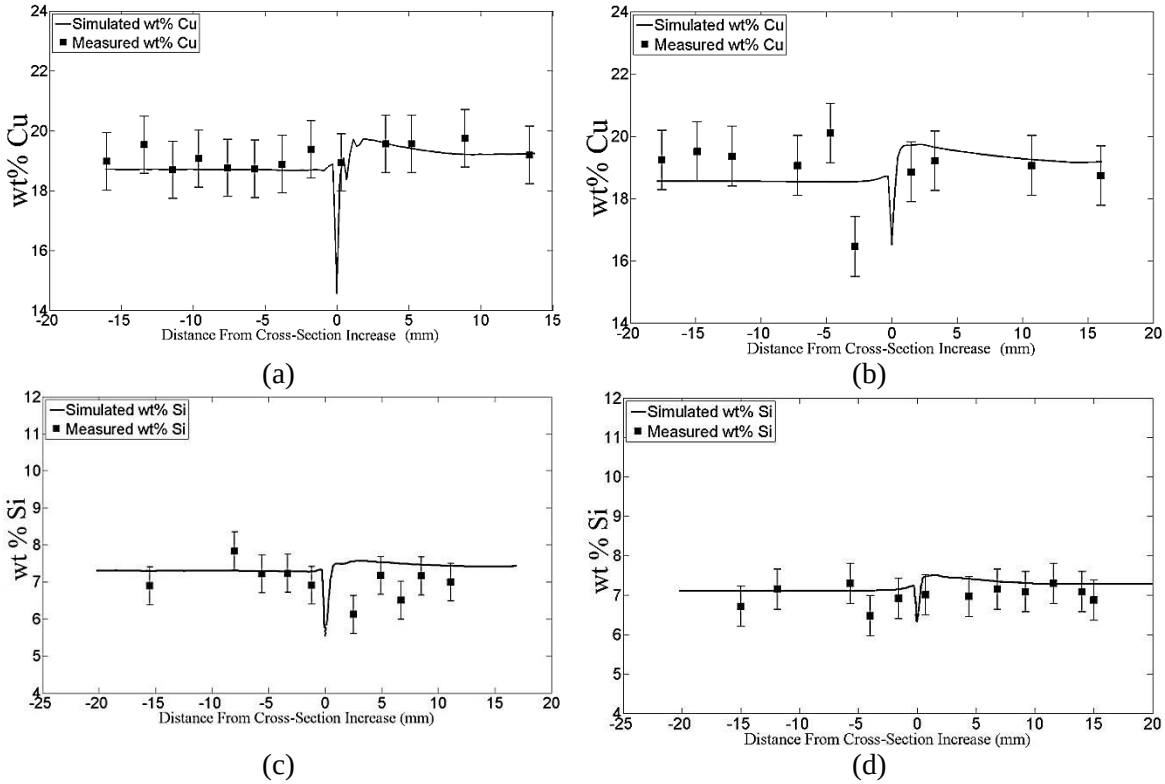

Figure 17: Longitudinal concentration distribution of directionally solidified Al-19Cu and Al-7Si close to the expansion: (a) Al-19Cu grown at 92 K cm^{-1}, 10 μm s^{-1}; (b) Al-19Cu grown at 53 K cm^{-1}, 29.1 μm s^{-1}; (c) Al-7Si grown at 40 K cm^{-1}, 10 μm s^{-1}; (d) Al-7Si grown at 51 K cm^{-1}, 29.1 μm s^{-1}.

3.3.3. Radial Macrosegregation in the Vicinity of Cross-section Expansion

3.3.3.1 Radial Macrosegregation in the Smaller Diameter Section before Expansion

Figures 18(a)-18(d) are plots for the measured radial macrosegregation in the smaller cross-section portion of Al-19Cu and Al-7Si samples grown at 10 and 29.1 μm/s. Ordinates are the ratio of local radial concentration of solute to the solute concentration within the entire cross-section; abscissas are radial fraction area solidified. Each subfigure shows radial macrosegregation profiles on two sections, one very close to the expansion and the other somewhat away from it. Distances from the expansion location are shown in the figures' legends; negative distance indicates that specimens are from places before the cross-section change.

Slower grown samples of both alloys show obvious radial macrosegregation (figs. 18(a) and 18(c)) where radial increase in the solute content is seen to occur starting around fraction area solidified of 0.5 indicating the strong mushy-zone steepling radially after that, while the faster grown ones in both cases show very small macrosegregation starting from higher area fraction solidified which implies that mushy-zones are relatively less steepled.

The other fact worthwhile mentioning is that if you compare figs. 18(a)-18(d) with those plotted in figs. 15(a)-15(d), respectively, the steeper radial macrosegregation profile is evident within the same samples in the smaller diameter portion, at locations close to the expansion (18(a)-18(d)) than in those right after the contraction (15(a)-15(d)), especially at slower growth speed. This could be because of the decrease in the intensity of the shrinkage flow close to the expansion; the larger melt pool above the expansion

location is feeding the solidification shrinkage while the shrinkage flow is stronger at the beginning of the narrow portion of samples. As seen before, shrinkage flow tends to flatten the mushy zone-liquid interface decreasing the degree of steepling and consequently reducing the radial macrosegregation; therefore, less intense shrinkage flow near the cross-section increase promotes less flattening of the convex interface, resulting in more radial macrosegregation. This is also explained below in figures 19(a) and 19(b) using a schematic representation of the interaction between various types of flows as the mushy-zone approaches the section increase, enters the expansion portion and then moves away from it into the larger constant cross-section portion above.

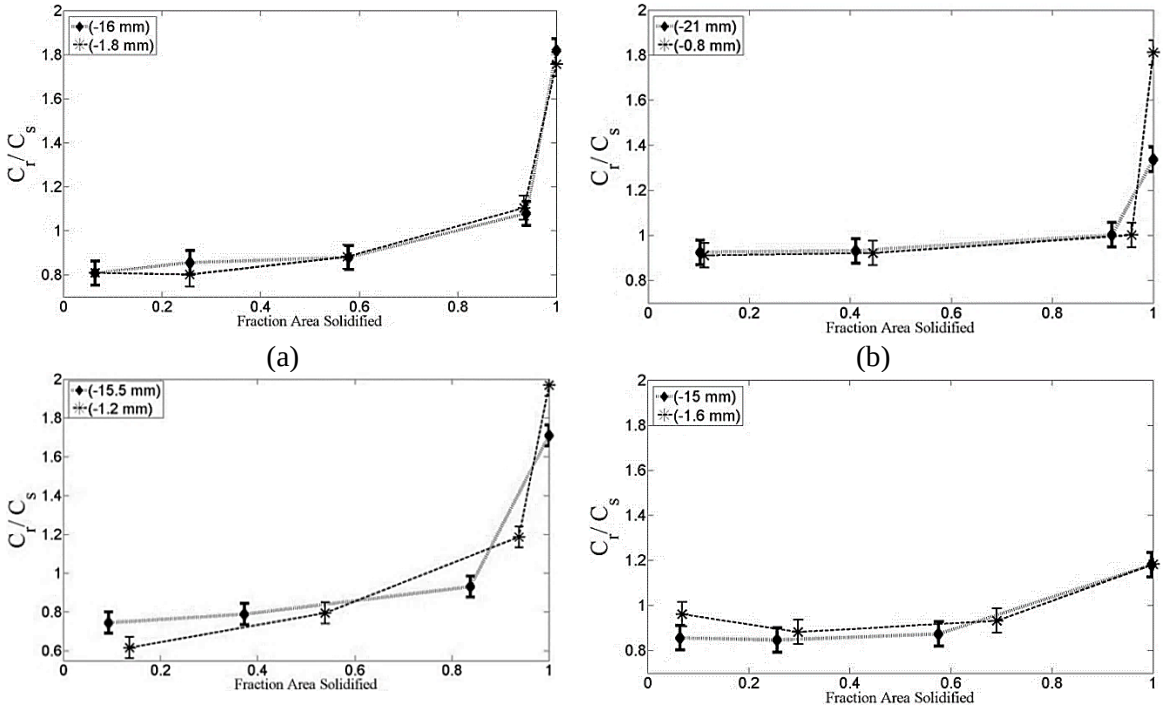

Figure 18 Experimental results of radial macrosegregation of Al-19Cu and Al-7Si directionally solidified out of an expansion. All the figures belong to the smaller sections before expansion: (a) and (b) correspond to Al-19Cu grown at 10 μm s^{-1} and 29.1 μm s^{-1}, respectively; (c) and (d) correspond to Al-7Si grown at 10 μm s^{-1} and 29.1 μm s^{-1}, respectively. Fraction area solidified is calculated from center of mass of the steepled dendritic array.

3.3.3.2. Radial Macrosegregation in the Larger Diameter Section after Expansion

Figures 19(a)-19(d) show schematic of the mold, mushy-zone and different flows in the expansion region. As discussed in the previous section, shrinkage flow intensity decreases when mushy-zone approaches the expansion, which results in the more steepled mushy-zone (compare the mushy-zone shapes in the smaller diameter portion in fig. 19(a) with 19(b)). As mushy-zone is coming out of the expansion, it mushrooms and extends sideways. At the same time, the steepling flow in the narrow portion advects solute-rich liquid outwards and upwards, and rolling over the expanding mushy-zone (fig. 19(c)). The interaction between the steepling flow from the narrow section below, expanding mushy-zone, and steepling flow forming in the larger diameter influence the macrosegregation pattern in this region. When the mushy-zone exits the expansion completely, steepled mushy-zone commensurate with the growth condition in the larger diameter section develops and continues to grow along the sample.

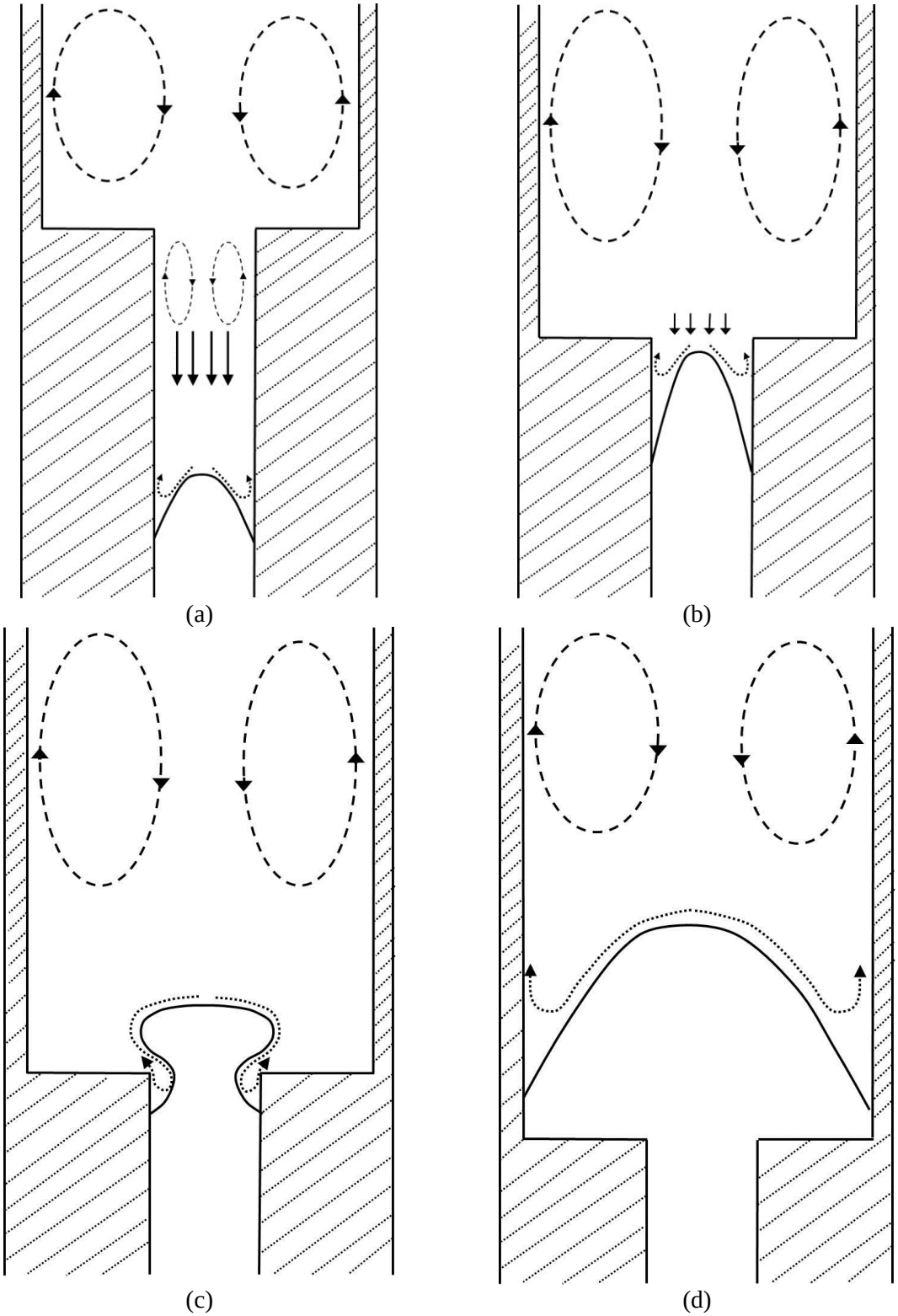

Figure 19: Schematic of the mold, mushy-zone, and different types of flows in the cross-section expansion region. Dashed circular arrows are thermal convection, solid arrows are shrinkage convection, and dotted rolling arrows are thermosolutal convection.

Figures 20(a)-20(d) plot the radial macrosegregation profile on specimens from larger diameter portions of Al-19Cu and Al-7Si samples grown at 10 and 29.1 μm/s, respectively. Each subfigure shows the profile for two cross-sections, one is the closest available to the expansion and the other is a couple of millimeters away from expansion. Ordinates and abscissas are similar to those in figures 18(a)-18(d).

Radial macrosegregation is present in both alloys and it is more severe in the slower growth speed (fig. 20(a) vs. 20(b) & fig. 20(c) vs. 20(d)); the low fraction solidified, corresponding to the core of the clustered dendrites, are solute depleted and solute content gradually increases towards the samples' periphery creating positive macrosegregation there. A closer look to the macrosegregation profiles reveals that the closest section to the expansion, in all the cases except fig. 20(a), is showing different behavior as compared to the section farther above it; these profiles are shown in red in figs. 20(a)-20(d). These red profiles show an increasing trend at low fraction solidified, then they remain relatively flat up to higher fraction area solidified, and finally increase to their final values near the edge of the samples creating an "S-shaped" profile versus the profiles farther above which are more like a parabolic profile (plotted in black). Below we will investigate the reasons for this behavior and explain the phenomena involved in producing this S-shaped solutal segregation profile. To this end, results from the simulations predicting solute concentration distribution were also employed to clarify the transition happening in the expansion region.

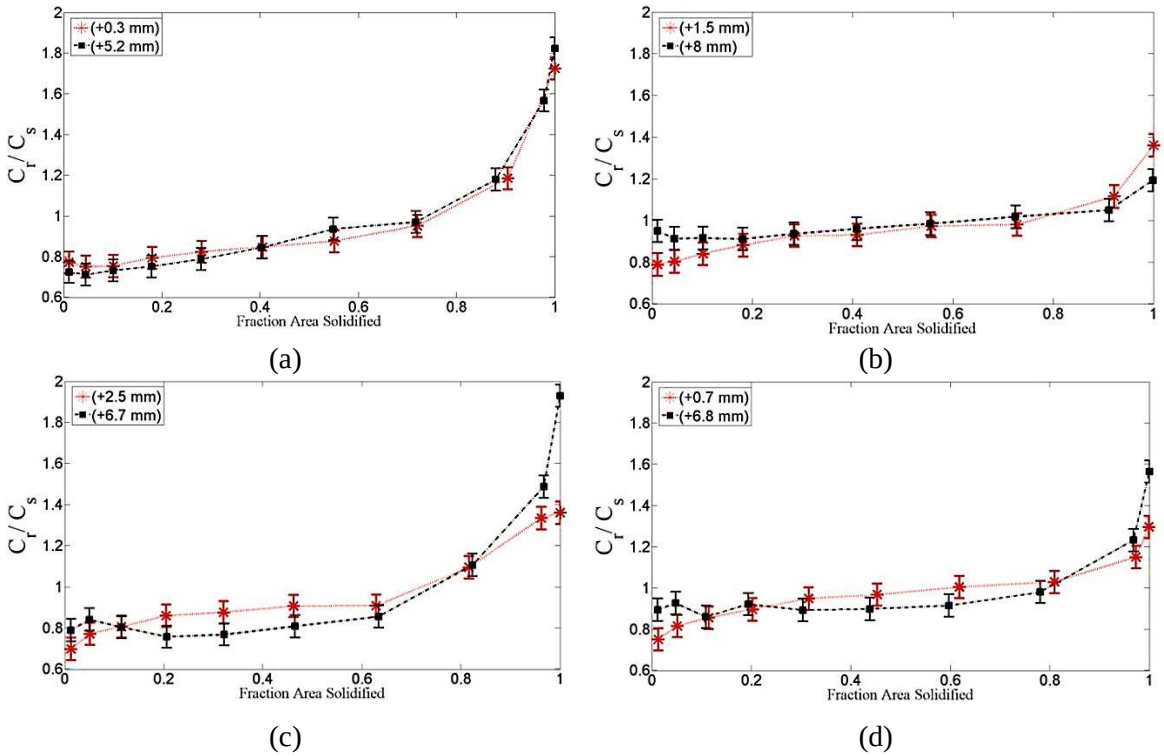

Figure 20: Experimental results of radial macrosegregation of Al-19Cu and Al-7Si directionally solidified out of an expansion in the larger diameter portion. All the figures belong to the larger sections after expansion; (a) and (b) correspond to Al-19Cu grown at 10 μm s^{-1} and 29.1 μm s^{-1}, respectively; (c) and (d) correspond to Al-7Si grown at 10 μm s^{-1} and 29.1 μm s^{-1}, respectively. Fraction area solidified is calculated from center of mass of primary α-phase.

Mushy-zones are already steepled in the small diameter portion of the mold and radial macrosegregation, commensurate with the growth conditions, exists; there is also solute inhomogeneity in the liquid right on top of the mushy-zone before the expansion. As the leading front of the mushy-zone exits the cross-section increase, it mushrooms and expands sideways, and new steeple in the larger diameter portion develops (see fig. 19(c)); thermosolutal convection sweeping solute outwards from the center is establishing. At the same time, solute-rich liquid from around the periphery of the smaller diameter section enters the larger diameter portion and is carried away by thermosolutal flow towards the mold walls in the larger diameter section. The degree to which the solute-rich liquid from the corners of the smaller diameter section is advected towards the

larger diameter edges depends on the strength of the thermosolutal convection, and on the solidification time.

Figures 21(a)-21(d) show the radial macrosegregation predictions from the simulations carried out at The University of Arizona. 21(a) and 21(b) are for Al-19Cu and 21(c) and 21(d) are for Al-7Si grown at 10 and 29.1 μm/s, respectively. Each subfigure plots the data corresponding to 0.2, 0.7 and 2.5 mm after the cross-section increase. The most noticeable point in these figures is the "peaked" radial macrosegregation profile at 0.2 mm after the expansion in all the cases. The peak location is at fraction area solidified of about 0.11, which corresponds to the ratio of the area of the smaller to larger diameter portions of the mold. The solid right after the cross-section increase is forming from two different liquids; the already segregated liquid from the smaller diameter portion coming out of the expansion—which radially occupies the area from the center up to 0.11 of the larger diameter portion's area—and the C_0 liquid preexisting on the expansion shelf. Therefore, radial macrosegregation profile shows solute depletion at the very low fraction area solidified, increases to the peak value corresponding to the macrosegregation in the smaller diameter section (at the fraction solidified of 0.11), followed by a relatively sharp decrease to the original liquid concentration extending all the way to the periphery of the mold. This behavior is evident in all the cases of figs. 21(a)-21(d) at 0.2 mm; the magnitude of the peaks are higher at slower growth speed indicative of stronger thermosolutal convection and more steepled mushy-zone before the expansion (figs. 21(a) vs. 21(b) & 21(c) vs. 21(d)). This solute-rich liquid is carried away outwards by the new thermosolutal convection forming there; the stronger this flow the sooner (distance-wise) it transitions to the steady-state radial

macrosegregation. As mentioned previously, the strongest thermosolutal flow occurs in the Al-19Cu alloy solidifying at 10 μm/s; also, the solidification time is about three-times of that in 29.1 μm/s. This strong flow forms the new steepled mushy-zone very soon, and long solidification time provides the opportunity of sweeping the solute towards the edges of the mold at shorter distance such that at 0.7 mm after the expansion the radial macrosegregation has almost reached to its steady-state parabolic-like profile (see fig. 21(a)). At 0.7 mm after the expansion in faster growth speed of Al-19Cu plotted in fig. 21(b), the radial macrosegregation is still in its transition and has an S-shaped profile. This means that the peaked profile in the weaker thermosolutal convection and where less solidification time is available requires longer distances to decay to its steady state profile seen at 2.5 mm.

Comparisons of figs. 21(a) and 21(c) shows that despite the similar solidification time, the radial macrosegregation is still in its transition state at 0.7 mm after expansion for Al-7Si grown at 10 μm/s, while greater solutal expansion coefficient in Al-19Cu, which creates stronger thermosolutal flow, leads to almost steady state profile at the same distance from the section-change. Radial macrosegregation profile at 0.7 mm for Al-7Si grown at 29.1 μm/s, seen in fig. 21(d), is slightly curvier than that in fig. 21(c); for example, at fraction area solidified of 0.4 the C_r/C_s is greater in faster growth speed than in slower one (fig. 21(c)). This means that at the same longitudinal distance and at the same fraction area solidified the solute content is more in faster growth speed, which is the indication of how stronger thermosolutal convection in slower speed results in the transition to steady-state radial macrosegregation to happen earlier (distance-wise). As expected, the simulations predict that at steady-state (profiles corresponding to 2.5 mm)

the degree of radial macrosegregation is higher at faster growth speed (fig. 21(a) vs. 21(b) or 21(c) vs. 21(d)).

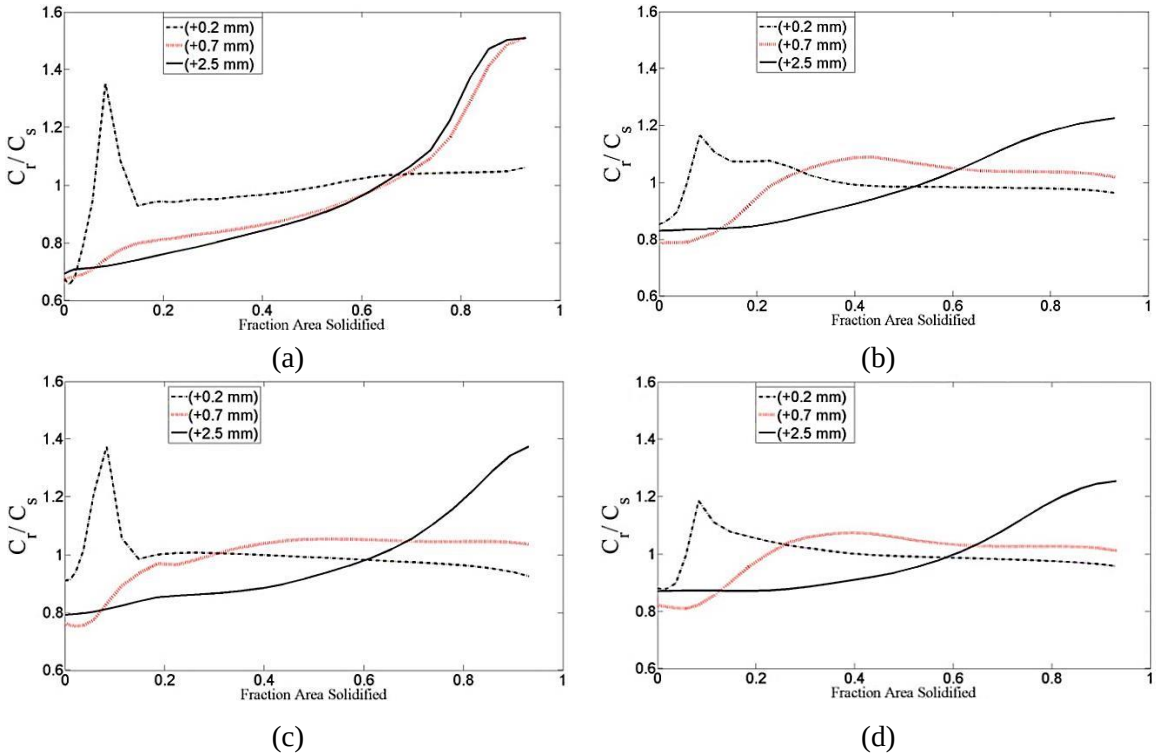

Figure 21: Simulation results of radial macrosegregation of Al-19Cu and Al-7Si directionally solidified out of an expansion in the larger diameter portion; (a) and (b) correspond to Al-19Cu grown at 10 μm s^{-1} and 29.1 μm s^{-1}, respectively; (c) and (d) correspond to Al-7Si grown at 10 μm s^{-1} and 29.1 μm s^{-1}, respectively. All the figures belong to the larger sections after expansion. Fraction area solidified is calculated from the center of the simulation domain.

Going back to figs. 20(a)-20(d) and by the help of insights gained by analysis of simulations' results, it is seen that at 0.3 mm after the expansion in Al-19Cu solidified at 10 μm/s (fig. 20(a)) the steady-state profile has already been reached and the peaked profile seen in simulation result is not seen; this is because of heavily steepled mushy-zone before the expansion, and of very strong thermosolutal convection developing soon after the section-change which advects copper to the outer edges. Simulations assumed a 2-dimensional domain which does not capture the entire 3-dimensional nature of the flow in the experiments and under-predict the flow strength. But, at 1.5 mm after the

expansion in the same alloy grown at faster speed (red curve in fig. 20(b)) obvious S-shaped radial macrosegregation profile is evident, which is an indication of being in the transition state at this distance, while at 8 mm above the expansion the regular (parabolic) steady-state radial macrosegregation profile resulted from the mushy-zone steepling is seen. Obvious S-shaped radial macrosegregation profiles, corresponding to the transition state, are seen at both 2.5 and 0.7 mm after the section-change in Al-7Si alloy solidified at 10 and 29.1 μm/s (see the red curves in figs. 20(c) and 20(d) respectively); but at locations farther away from expansion the steady-state macrosegregation has reached.

3.4. Spurious Grain Formation after Cross-section Expansion

Formation of misoriented grains (spurious grains) as the liquid-solid interface moves into the larger cross-section of the mold is a serious problem for single crystal turbine blade casting industry and has been extensively reported in the literature. When the primary dendrite array growing in the smaller cross-section below enters a larger cross-section region above, the dendrite side-arms (secondary branches) grow and spread side-ways to fill the mold cavity [30]. The tertiary branches growing off of these secondary arms then become new primary arms. Since, the face centered metal alloys growing along [100] direction grow the four orthogonal side arms along <100> directions these tertiary branches are expected to maintain the same [100] orientation as the other primary dendrites in the array. This would result in the entire length of the turbine blade having a [100] orientation. However, due to more efficient heat extraction associated with corners, the melt can locally undercool there and result in the nucleation of new randomly orientated grains [30]; corners are therefore further considered as favorable

heterogeneous nucleation sites. This has been the main mechanism used to describe the formation of spurious grains in directionally solidified single crystal turbine blade components [30, 40-42]. However, fragmentation of slender and fragile side-branches can also be caused by thermosolutal and shrinkage driven convection associated with solidification through the cross-section changes, which can also lead to the formation of spurious grains during directional solidification. There is ample evidence that dendrite fragmentation does occur during directional solidification [43-45], especially when there is a sudden decrease in the growth speed [43, 44].

In this research, the mold material and design have been selected such that the melt undercooling on the corners of expansion platform does not occur. Unlike the constant wall thickness ceramic molds used by investment casting industry [30] where during directional solidification the melt undercooling is expected to occur at the platform corners just above the section increase, our molds were made of graphite and since the crucibles had a constant outer diameter the wall thickness of the mold in the larger cross-section above the expansion is less than the wall thickness in the smaller cross-section below, 4.5 mm vs. 7.8 mm. Graphite is less heat-conductive as compared to the both liquid and solid phase metallic alloys used; decreasing the mold thickness after the expansion and increasing the amount of melt there, lead to more efficient inward heat flow in that region. This locally bends the isotherms towards the all-liquid region above even more, meaning that the temperature increases near the outer edges of the larger diameter section as compared to the central regions. Thus, the liquid at the corners of the expansion shelf is not expected to undercool.

Figures 22(a)-22(d) are exactly the same as figs. 16(a)-16(d) except the top part of figs. 22(a) and 22(b), which correspond respectively to the transverse microstructures of Al-19Cu grown at 10 and 29.1 μm/s, show the grain boundaries marked with red ink for improved visualization. It is evident from these images that the grain existing in the narrow portion of the mold below (seen in the bottom part of figs. 22(a) and 22(b)) grew and occupied the central region in the larger cross-section portion above. However, several additional new grains (spurious grains) are also seen in the larger cross-section above for the Al-19Cu alloy. It is interesting to note that this is not the case with the Al-7Si samples. In the Al-7Si alloy, grown at both speeds, the same grain from the smaller diameter section grew and filled up the entire larger cross-section after the expansion (figs. 22(c) and 22(d)); no spurious grain formed.

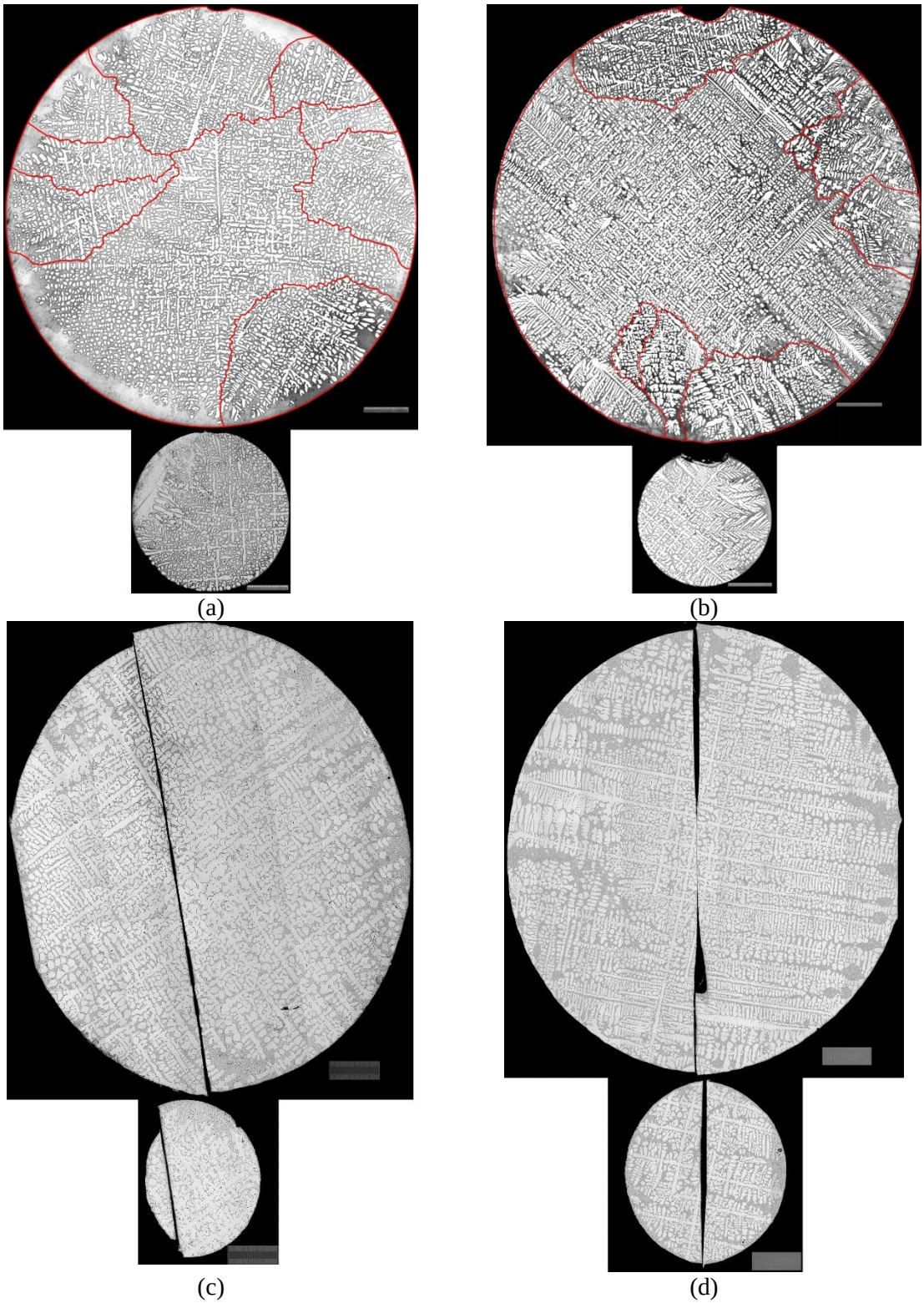

Figure 22. Transverse microstructures of directionally solidified Al-19Cu and Al-7Si before and after a cross-section increase with the grain boundaries drawn on the microstructures after the expansion. (a) and (b) are Al-19Cu with the grain boundaries drawn on the microstructures after the expansion; (c) and (d) are Al-7Si. Scales are 1 millimeter.

For more detailed study of the microstructures in the vicinity of the expansion, longitudinal cuts were made through the expansion regions of these samples. Figures 23(a) and 23(b) show longitudinal microstructure of Al-19Cu grown at 10 and 29.1 μm s^{-1}, and figs. 23(c) and 23(d) are for Al-7Si grown at 10 and 29.1 μm/ s, respectively. There is extensive formation of misaligned dendrites after the expansion in the Al-19Cu samples (red arrows are drawn along the length of these misaligned dendrites). But in the case of Al-7Si alloy, it appears that the primary dendrites maintained their [100] orientation from the smaller diameter below and grew side-ways to fill the larger section above without the formation of any spurious grain. Also, the misaligned dendrites in the larger diameter section of Al-19Cu samples appear to have formed at the re-entrant corners and not at the outer periphery of the larger diameter section as would be suggested by the mechanism of "new grains nucleating in an undercooled melt in response to the local thermal profiles at the sharp corners".

Before further discussion about the formation of spurious grains, let's go back to figs. 17(a)-17(d) where the longitudinal macrosegregation in the expansion region are plotted. Simulations predicted that there are negative macrosegregation right on top of the cross-section increase platform, but since there were no transverse cut available very close to the expansion, no data point was plotted there. But, the longitudinal microstructures (figs. 23(a)-23(d)) clearly indicate that almost pure primary α-phase, with low solute content, formed right on the top of the expansion shelf in all these cases. This is an evidence of the severe negative segregation right after the section increase indicated by the simulation results in figure 17(a)-17(d).

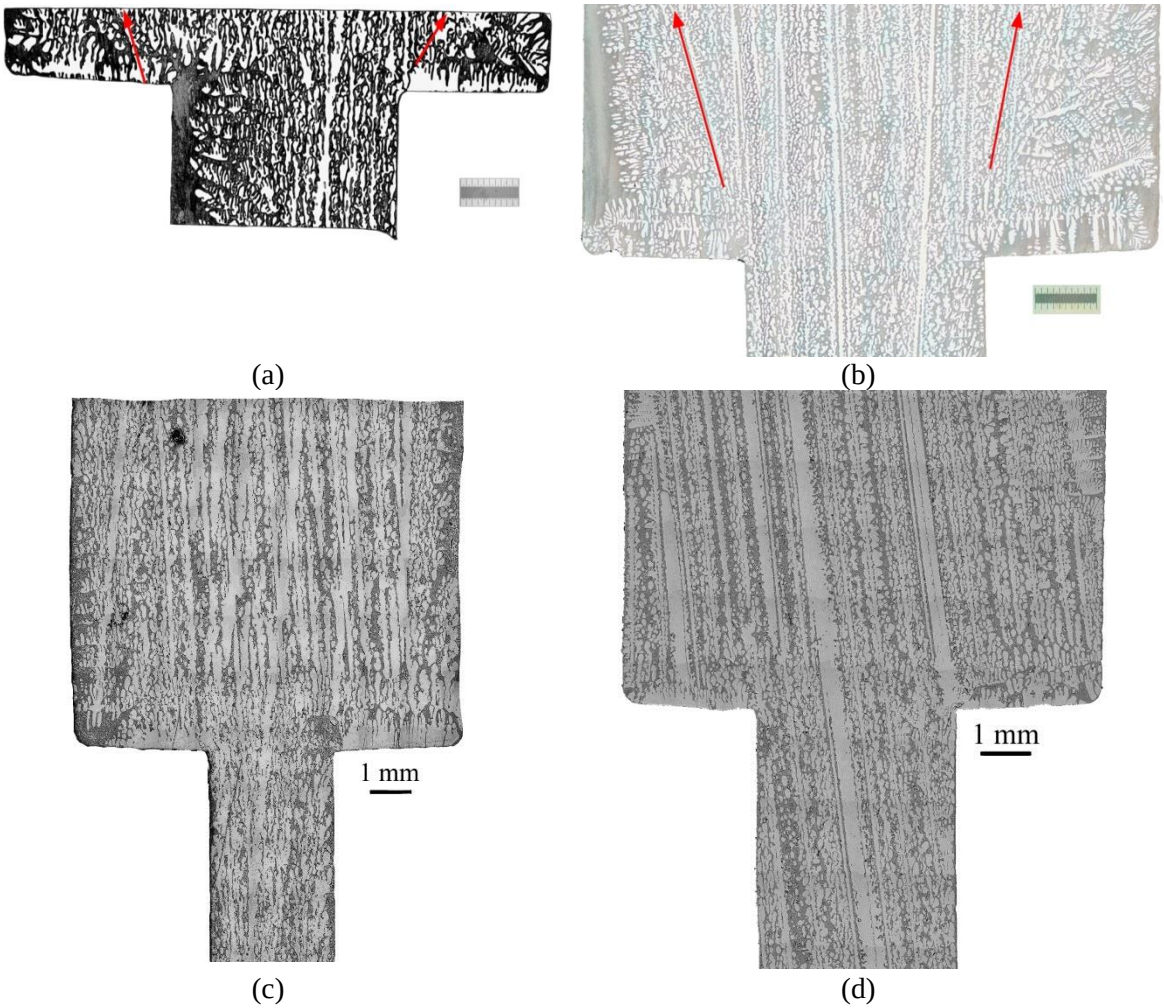

Figure 23: Longitudinal microstructures of Al19Cu and Al-7Si in the expansion region. (a) is for Al-19Cu solidified at 92 K cm^{-1}, 10 µm s^{-1} and (b) is for Al-19Cu solidified at 53 K cm^{-1}, 29.1 µm s^{-1}, red arrows show the direction of new misoriented dendrites formed after the expansion. (c) is for Al-7Si solidified at 40 K cm^{-1}, 10 µm s^{-1} and (d) is for Al-7Si solidified at 51 K cm^{-1}, 29.1 µm s^{-1}.

Below, we will examine the nature of thermosolutal convection in the vicinity of cross-section increase in the Al-19Cu and Al-7Si alloys grown at two growth speeds, and explore the possibility of dendrite fragmentation due to solutal remelting as the cause of the observed "spurious grain" formation. As explained earlier, the "steepling" thermosolutal convection is dominant in this region; and it is much stronger in Al-19Cu as compared to Al-7Si grown under similar conditions. It was also shown that the secondary branches of the primary dendrites near the outer portion of the "steepled"

region are longer because they extend sideways and the tertiaries growing off of these side arms are quite slender (see the transverse microstructures right after the expansion in figs. 22(a)-22(d) where long secondary dendrites and slender tertiaries perpendicular to them are shown). If the thermolsoutal convection can bring in solute rich melt towards these slender tertiary arms then local remelting is likely to occur at their root resulting in fragmented dendrite pieces which can grow and become new misoriented grains.

We will use the parameter identified by Mehrabian *et al*. [46] for our proposed potential solutal remelting mechanism in the mushy-zone, $\frac{v\,.\nabla T}{\varepsilon} < -1$, where v is the liquid velocity, ∇T is the thermal gradient and ε is the local cooling rate. This criterion implies that if the solute-rich liquid is flowing up the thermal gradient faster than the velocity of the isotherm it can lead to solutal remelting of the solid dendrites already existing there. The $\frac{v\,.\nabla T}{\varepsilon}$ values from the simulation results were used to plot figures 24 (a)-24(d) near the cross-section expansion to assess the possibility of dendrite remelting in our experiments due to thermosolutal convection. Fig. 24(a)-24(d) are plots of the Mehrabian criterion for the Al-19Cu and Al-7Si in the expansion region when part of the mushy-zone exited the cross-section increase; because of the symmetry only the magnified left-half of each case is plotted. Figures 24(a) and 24(b) are for Al-19Cu, and 24(c) and 24(d) are for Al-7Si grown at 10 and 29.1 μm s^{-1}, respectively. In these figures, vectors show liquid velocity, dashed red lines denote isotherms, in K, blue lines represent isopleths of fraction liquid, white region is the graphite mold, and the colored background represents the Mehrabian's parameter. Inside the envelopes, bounded by $\frac{v\,.\nabla T}{\varepsilon} = -1$ isopleth drawn by solid black lines, are the regions where the parameter is less than -1.

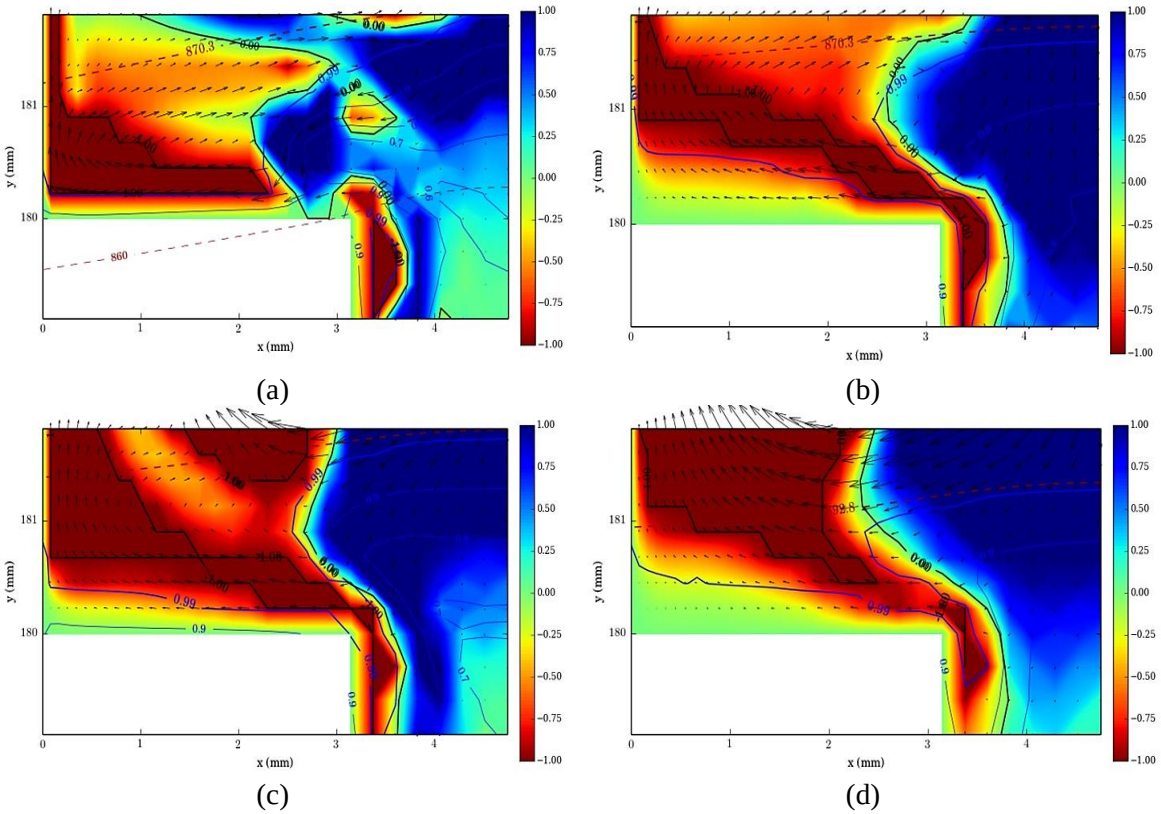

Figure 24: Steepling front coming out of expansion with the Mehrabian criterion plotted in the mushy zone; arrows are velocity vectors. Regions bounded with solid black lines are locations where Mehrabian criterion is less than -1 and the solutal remelting of dendrites is likely in those regions.

The top of the steepling front is seeing fluid flow anti-parallel to the velocity of the isotherms which results in a positive Mehrabian parameter and a rapid increase in the solid fraction. On the sides and near the re-entrant corner, the parameter is negative and is less than -1 inside the envelops mentioned earlier, showing that the fluid flow here is inhibiting solidification by bringing solute enriched fluid to the area. Therefore, the likelihood of solutal remelting, and consequently fragmentation of dendrites is high in these regions.

If the root of a secondary or tertiary dendrite arm is dissolved, it is possible for it to develop into a stray grain, especially if it floats up and rotates into to a better orientation for its growth with respect to the local thermal gradient. If it sinks then it is

likely to be trapped within the growing dendrite array and may not develop into a new spurious grain. Primary α-phase dendrite fragments have been observed to float in the melt in hypoeutectic Al-Cu alloys ranging from 20 to 30 wt. % Cu, during solidification and sudden decrease in the growth speed, clearly indicating that the density of these fragments is less than the alloy melt surrounding them [47, 48]. For the Al-7Si alloy, however, that is not the case. Magnusson *et al*. measured the Al-Si alloys density ranging from 3 to 11.6 wt. % Si [49] and showed that the density of the solid was more than that of the liquid alloy. Since the Al-19Cu dendrite fragments are likely to float in the melt they are more likely to produce spurious misoriented grains than the Al-7Si dendrite fragments, which are likely to sink and get trapped in the array. This is in agreement with our experimental observations discussed above. As mentioned earlier, because of the strong thermosolutal convection in the Al-19u alloy, mushy-zone steepling and side-ways spreading of the dendritic structure happen very soon after the expansion; this is while solute-rich liquid from lower temperature locations around the periphery of smaller diameter section below comes in contact with newly formed thin secondary and tertiary dendrites (see schematic drawn in fig. 19(c)). This upwards flow makes Mehrabian's parameter smaller than -1 near the re-entrant corners (figs. 24(a) and 24 (b)), and since this flow brings enriched liquid to the region the likelihood of solutal remelting and fragmentation is extremely high there.

It is also interesting to compare the longitudinal microstructure shown in figures 23(a) and 23(b) and the Mehrabian parameter plot in figures 24(a) and 24(b). The Mehrabian parameter indicates that re-entrant corners and not the platform edges are the likely places for dendrite fragmentation; these are precisely the locations of the

experimentally observed formation of stray-grains. Careful electron backscatter diffraction (EBSD) examination on longitudinal microstructures of Al-7Si samples, shown on figure 25(a) and 25(b) for growth speed of 10 and 29.1 μm/s respectively, also shows “trapped” misoriented dendrite fragments (see the magnified portions on each figure). This indicates that in Al-7Si alloys also thermosolutal convection causes dendrite fragmentation, but these fragments get entrapped in the growing dendrite array and do not develop into a new grain.

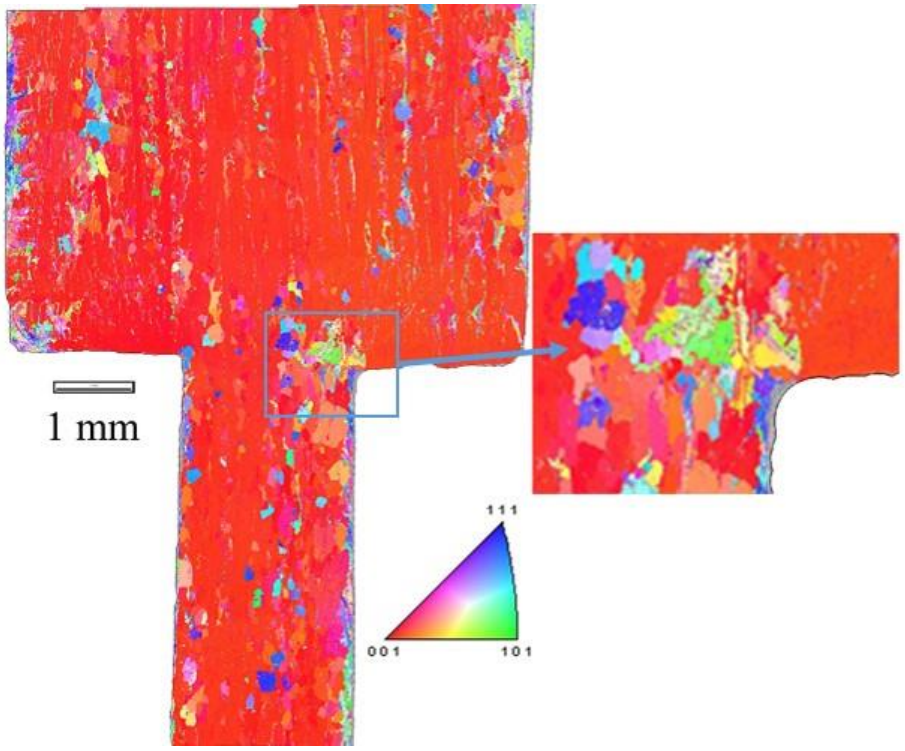

(a)

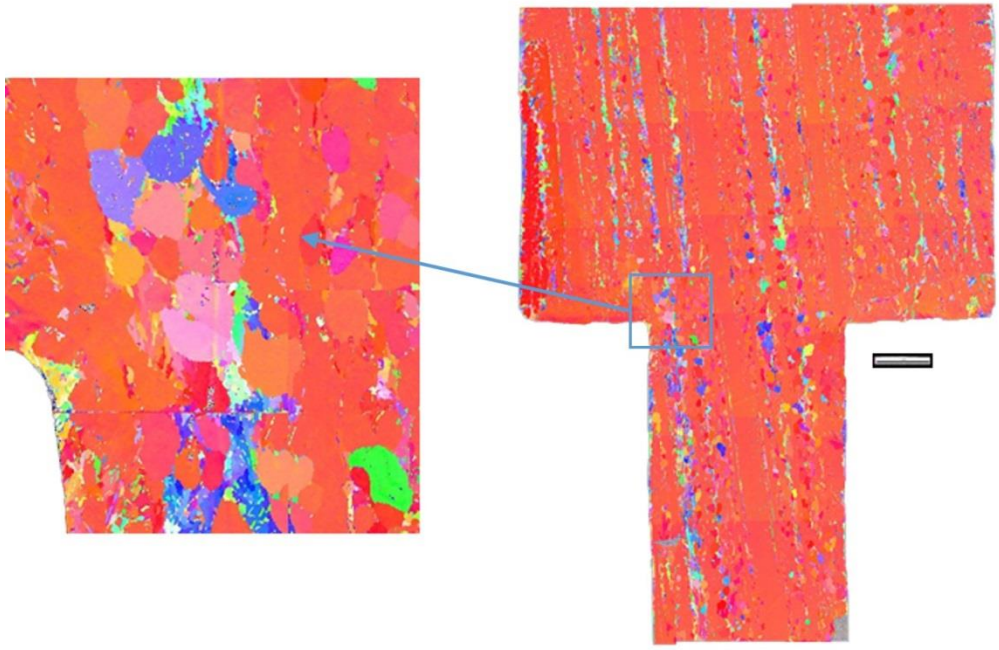

(b)

Figure 25: EBSD analysis of the longitudinal microstructure of Al-7Si alloys grown at (a) 10 μm/s and (b) 29.1 μm/s. The colore-coded map represents the crystallographic directions.

3.5. Morphological properties of dendritic array during directional solidification

There are several measures used to quantify the morphology of dendritic array, like primary dendrite arm spacing, dendrite shape factor, dendrite spacing as determined by minimum spanning tree, primary dendrite trunk diameter, secondary arm spacing, to name a few. In this research, primary dendrite arm spacing and primary dendrite trunk diameter are studied. Due to the lack of strong models and possibility of simulation of morphological behavior of dendrites (because of its complexity), the effects of processing conditions on them are not widely known; this section primarily presents the experimental data and makes some rough comparisons with some simple models predicting primary dendrite arm spacing and primary dendrite trunk diameter.

3.5.1. Primary dendrites arm spacing

Modeling mushy-zone morphology during directional solidification is quite difficult because of the length scales involved; dendrite tip radius is ~ micrometer, the primary spacing is ~0.1 mm, and mushy zone height is ~cm. Presence of thermosolutal convection makes the analysis even more complex and non-linear, the array morphology determines the nature of convection and the nature of convection determines the array morphology. There have been some efforts in modeling dendrite tip radius, primary dendrite arm spacing and tip composition based on several simplifying assumptions such as diffusive transport of mass and heat (convective transport is ignored) and simple needle-shape dendrites structure [6, 50-53]. There have also been some numerical simulations of dendrites morphology considering convection within the mushy-zone; but they include several assumptions about the moving liquid-solid interface [54-56].

There are semi-theoretical models developed to predict some morphological properties like dendrite tip radius and primary dendrites spacing [50-53]; the most popular one is Hunt-Lu model which combines theoretical models with experimental polynomial fits. This model has been widely used by researchers, and showed to be valid over a wide range of compositions, growth speed and thermal gradients. In this research, the Hunt-Lu model is used to calculate the primary dendrite spacing.

Primary dendrites arm spacing is calculated by using equation (10) below

$$\lambda = \frac{\lambda' \Gamma k}{\Delta T_0}$$

in which k is solute partition coefficient, Γ is Gibbs-Thompson coefficient and $\Delta T_0 = \frac{mC_0(k-1)}{k}$, where m is the phase diagram liquidus slope and C_0 is the original bulk liquid composition. λ' is a dimensionless parameter defined below:

$$\lambda' = 0.07798 V'^{(a-0.75)} (V' - G')^{0.75} G'^{-0.6028}$$

where

$$V' = \frac{V \Gamma k}{D_l \Delta T_0}$$

with V as growth speed and D_l as solute diffusion coefficient in the liquid phase; and

$$G' = \frac{G_l \Gamma k}{\Delta T_0^2}$$

with G_l as the thermal gradient, parameter "a" is as follows,

$$a = -1.131 - 0.1555 \log_{10} G' - 0.007589 (\log_{10} G')^2$$

Table III shows the parameters and thermophysical properties of both alloys used in the calculations based on Hunt-Lu model.

Table III: Parameters and thermophysical properties used in Hunt-Lu model for calculating primary dendrite spacing, and in Tewari model for calculating trunk diameter.

	k	m_l (K/wt. %)	Γ (K.m)	D_l (m^2/s)
Al-19Cu	0.1203	-3.3429	1.976×10^{-7}	5.388×10^{-9}
Al-7Si	0.1273	-6.9468	1.702×10^{-7}	5.409×10^{-9}

As explained in section 2.6, with its details available in the Appendix, Nearest Neighbor Spacing (NNS) for each dendrite and their average within each transverse microstructure were calculated. Figures 26(a) and 26(b) plot the average measured NNS within cross-sections and those predicted by Hunt-Lu model for Al-19Cu samples grown at 10 and 29.1 μm/s, respectively, in the contraction region; figures 26(c) and 26(d) are similar to 26(a) and 26(b) but for Al-7Si samples grown at 10 and 29.1 μm/s, respectively. Ordinates are NNS in micrometer, and abscissas are the distance of transverse sections from cross-section contraction in mm.

Measurements do not show any trend either based on the growth speed or on the effect of cross-section change; for both alloys and both growth speeds the NNS values before and after contraction are within the standard deviation of data and no indication of effects of section-change on the values is seen. But, the average of NNS for Al-7Si samples are higher than that for Al-19Cu grown at similar conditions (fig. 26(c) and 26(d) versus fig. 26(a) and 26(b)). Predictions seen in figures 26(a)-26(d), however, show that in both alloys the slower grown samples have higher primary dendrites spacing; it

also predicts higher values for the Al-7Si samples as compared to Al-19Cu grown at the same speed. The average spacing predicted by the model (which accounts only for the diffusion transport) is greater than that experimentally measured; it appears that the dendrites clustering due to steepling in actual experiments is the reason for the primary dendrite spacing to be smaller, and the spacings to be very similar at both growth speeds. The NNS prediction for Al-7Si grown at 29.1 μm/s, however, is in a good agreement with the experimentally measured values (see fig. 26(d)); this is the case with the weakest steepling convection, therefore it is closer to the diffusion controlled transport which is the assumption of the Hunt-Lu model.

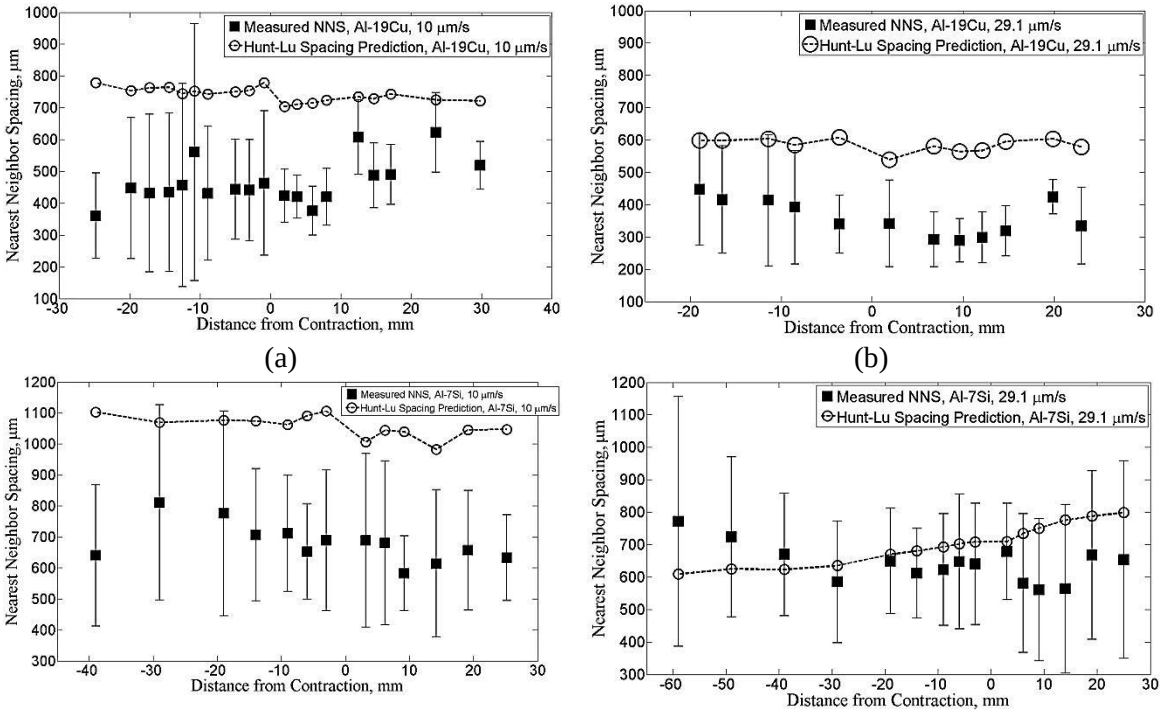

Figure 26: Experimentally measured Nearest Neighbor Spacing (NNS) and predicted primary spacing by Hunt-Lu model for sections before and after contraction.

Figures 27(a)-27(d) are similar to those in figures 26(a)-26(d), but they plot the measured NNS and predicted primary dendrite spacing for the sections before and after

the expansion in cross-sections. They do not show any effect of growth speed or cross-section increase on NNS; but higher values for Al-7Si samples grown at similar conditions to Al-19Cu samples are evident (compare fig. 27(c) and 27(d) with 27(a) and 27(b)). The corresponding Hunt-Lu spacing calculations, however, predict larger spacing for the samples grown at slower speed in both alloys. The average predicted spacings, in both alloys and both growth speeds, are greater than the measured ones; steepling resulted from thermosolutal convection is assumed to be responsible for this difference. Again, the predicted values of primary dendrite spacing for the Al-7Si grown at 29.1 μm/s is the closest to the actual measurements, fig. 27(d); this is attributed to the less steepled mushy-zone and less clustered primary dendrites in this case.

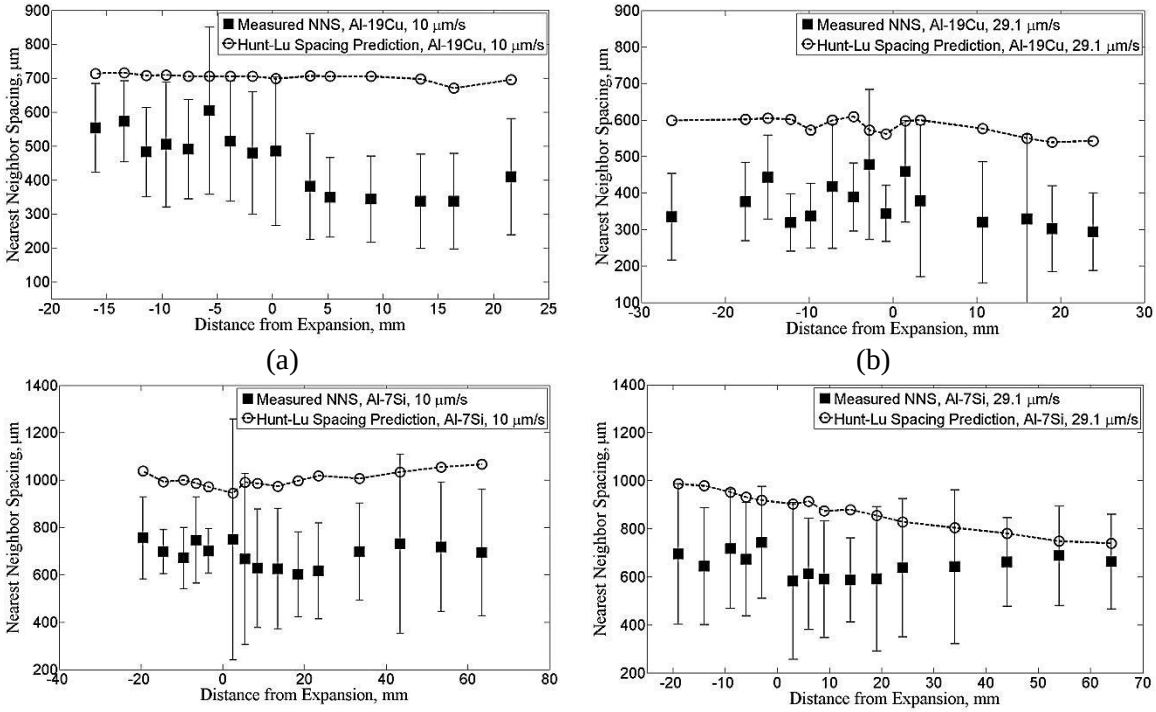

Figure 27: Experimentally measured Nearest Neighbor Spacing (NNS) and predicted primary spacing by Hunt-Lu model for sections before and after expansion.

3.5.2. Primary dendrites trunk diameter

Trunk diameter measurements on several transverse microstructure of both Al-19Cu and Al-7Si samples were performed as explained in the section 2.6. The average trunk diameter on each section was then calculated. Tewari et al. [57] proposed a semiemperical model based on the Kirkwoods' work [58] for prediction of the primary dendrite trunk diameter in directionally solidified alloys; equation (10) below shows the relationship between the trunk diameter and processing conditions with thermophysical properties.

$$\phi^3 = 96\frac{D_l\,\Gamma}{VG(1-k)}\ln\left\{\frac{1+\frac{VGt}{m_lC_0}}{1+\frac{VGt_0}{m_lC_0}}\right\} + \phi_0^3 \qquad (10)$$

In this equation ϕ is the predicted trunk diameter, $\phi_0 = 6.59r_t$ (with r_t being the dendrite tip radius calculated from Hunt-Lu models [50]) is the initial trunk diameter, D_l is the solute diffusion coefficient in the liquid, V is growth speed, G is thermal gradient, Γ is Gibbs-Thompson coefficient, k is solute partition coefficient, m_l is liquidus slope, and C_0 is the alloy composition. In equation (10), $t = \frac{m_l(C_E - C_0)}{VG}$ is the alloy freezing time and $t_0 = \frac{22r_t}{V}$ is the initial trunk growth time.

Figures 28(a)-28(d) plot the experimentally measured and theoretically predicted trunk diameter values within transverse sections of Al-19Cu and Al-7Si samples for both before and after contraction. Ordinates are trunk diameter in micrometer and abscissas are the distance from cross-section decrease. Figures 28(a) and 28(b) are for Al-19Cu samples grown at 10 and 29.1 μm/s, respectively, and 28(c) and 28(d) are for Al-7Si samples grown at 10 and 29.1 μm/s, respectively.

Contrary to what was seen in the measured NNS in the contraction region (figs. 26(a)-26(d)), measured trunk diameters are distinguishable based on the growth speed; in both alloys the trunk diameters of the slower grown sample are bigger (fig. 28(a) vs. 28(b) and 28(c) vs. 28(d)); Al-7Si samples, however, have larger trunk diameter as compared to the Al-19Cu grown at the same speed (compare values plotted in fig. 28(c) with those in 28(a), and 28(d) with those in 28(b)). There appears to be an increase in the average trunk diameter values of specimens corresponding to the first cut after the contraction in both alloys and both growth speeds (see the values corresponding to right before and right after the cross-section decrease location). As explained earlier, solute depleted central region of the mushy-zone enters the contraction and forms the final low concentration solidified alloy at that location (see figs. 13(a)-13(d) for the longitudinal negative macrosegregation right after cross-section decrease); trunk diameters of a dendritic array formed from a lower concentration alloy are larger. The increase in the trunk diameter could be attributed to this fact.

The predicted values of trunk diameter for Al-19Cu grown at 10 μm/s plotted in figure 28(a) are in good agreement with the experimentally measured ones; but this is not true for the Al-19Cu grown at 29.1 μm/s plotted in figure 28(b). The predictions, also, show larger trunk diameters for the samples grown at 10 μm/s than those grown at 29.1 μm/s (compare open circles in figs. 28(a) and 28(c) with those in fig. 28(b) and 28(d) respectively); this is consistent with experimental observations. In both alloys and both growth speeds, the prediction of trunk diameter at the locations right after the contraction shows an increase (see the symbols corresponding to the first positive distances and

compare them with the first ones right before the contraction); this is also consistent with what was seen in the experimentally measured values for trunk diameter.

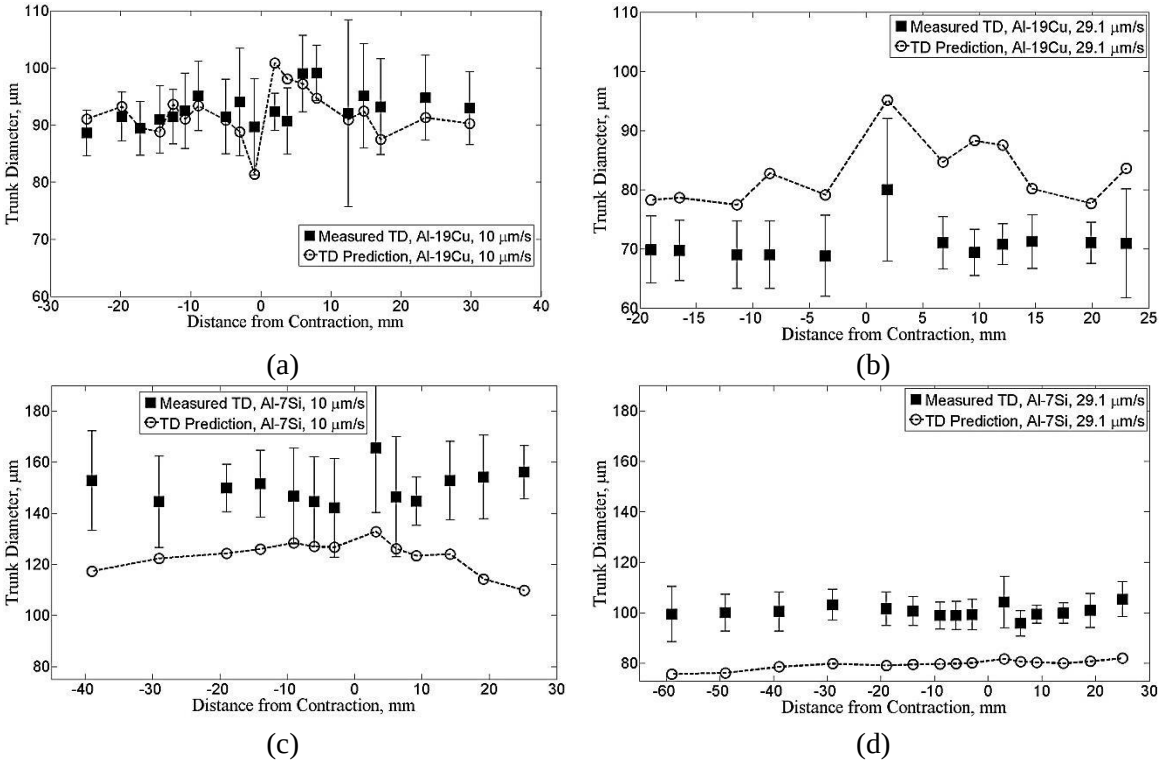

Figure 28: Experimentally measured and theoretically predicted Trunk Diameter (TD) using equation (10) for sections before and after contraction.

The average of measured trunk diameters on sections before and after expansion are plotted in figures 29(a)-29(d) for Al-19Cu and Al-7Si samples grown at both speeds. Al-7Si samples have larger trunk diameters as compared to Al-19Cu solidified at the same speed (compare values plotted in fig. 29(c) and 29(d) with those in 29(a) and 29(b) respectively). But, no trend because of cross-section change is seen in either case. Also, similar to what was seen in figs. 28(a)-28(d), the slower grown samples have larger trunk diameters.

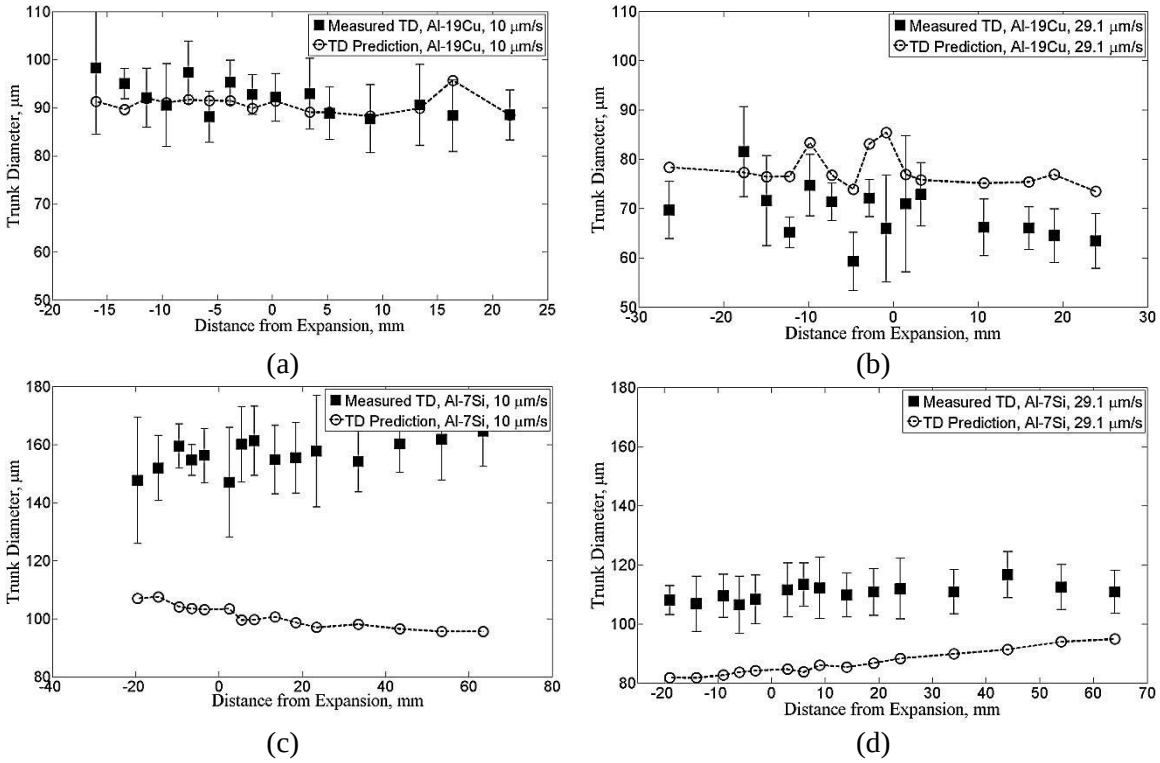

Figure 29: Experimentally measured and theoretically predicted Trunk Diameter (TD) using equation (10) for sections before and after expansion.

Trunk diameter appears to be a more responsive morphological property as compared to primary dendrite spacing so far as the response of array morphology on the local changing processing conditions is concerned. But, since mushy-zone steepling results in dendrites getting clustered together, growth speed dependence of primary dendrite spacing is not evident from the experimental data. Moreover, presence of different grains and formation of spurious grains introduces errors in the NNS measurements. Therefore, any study of primary dendrite spacing requires a single grain dendritic microstructure; however, trunk diameter is more responsive to the local processing conditions and can be studied with more scrutiny.

Chapter IV

Summary

Al-7Si and Al-19Cu alloys were directionally solidified at 10 and 29.1 μm/ s in 30 cm long 18.4 mm outer diameter cylindrical graphite mold having abrupt inner diameter increase (3.5 to 9.5 mm) and also abrupt inner diameter decrease (9.5 mm to 3.5mm). Effect of thermosolutal convection on the longitudinal and radial macrosegregation was examined in the vicinity of section-change. Effect of section-change on the primary dendrite spacing and trunk diameter was also studied. Following observations have been made under this research.

1. Directional solidification in constant cross-section mold: Despite the fact that the interdendritic liquid of the alloy systems studied, Al- 19 wt. % Cu and Al- 7 wt. % Si, is thermally and solutally stable against the buoyant forces when directionally solidified upwards with respect to gravity, inevitable radial thermal gradient creates *thermal convection* cells in the all-liquid region above the mush-zone. Therefore, hotter liquid near the mold's wall flows upwards and cooler liquid in the interior

flows downward. This favors dendritic growth in the central regions, which results in the flow of denser liquid in contact with the tips of the leading dendrites diagonally downwards on to the lagging neighbors. Mushy zone-liquid interface, consequently, becomes *steepled* or convex towards the all-liquid region above. These steepled mushy-zones have been observed in directionally solidified Al-Ni [15], Al-Cu [11] and Pb-Au [13] alloys. The thermosolutal convection associated with this phenomenon is called *steepling thermosolutal convection* which advects solute-rich liquid sideways towards the samples periphery increasing the solute concentration there and leaving the central region solute-depleted. As a result of this, on the transverse microstructures primary dendrites are clustered in the interior portion while the regions close to the mold walls contain high solute content eutectic-rich microstructure. This research showed that the radial macrosegregation profiles in the constant cross-section portions of the samples are of the *parabolic-shape*, because of the steeple center being solute poor and steeple periphery being solute rich. The degree of radial macrosegregation for both alloys was observed to be higher at slower speed. About 20 times larger coefficient of solutal expansion in Al-19Cu as compared to that in Al-7Si creates much stronger steepling convection in this alloy; hence, the radial macrosegregation was observed to be more severe in Al-19Cu than in Al-7Si samples grown under similar conditions.

2. Directional solidification through an abrupt cross-section decrease: The solute-enriched liquid at the outer periphery of the larger cross-section portion of the sample gets entrapped as the central protruding portion of the dendrite arrays moves into the smaller diameter portion above. This results in a positive macrosegregation along the

sample length just before the section decrease. Solute-depleted central portion of the steepled mushy-zones entering the smaller diameter portion of the mold above creates a negative macrosegregation just above the section decrease. Therefore, a positive macrosegregation right before the contraction, in the larger diameter portion, followed by a negative macrosegregation, right after in the smaller diameter section above, was observed in both alloys. The extent of these macrosegregations, however, are larger at the slower grown samples, and are greater in the Al-19Cu samples in comparison to Al-7Si grown at similar conditions.

Since the shrinkage flow, feeding solidification shrinkage, is intensified in the contraction region because of the area-reduction, this *area-change-driven-shrinkage flow* brings C_0 liquid into the solidifying mush when it is closer to the contraction; solute-depleted central portion of the dendritic array is remelted, therefore the mushy-zone gets flattened and the radial macrosegregation profile changes from being parabolic-shaped to *S*-shaped. The faster the growth speed the stronger the shrinkage flow, and therefore the deeper in the mushy-zone the effect of this flow is observed. On the other hand, the more steepled the mushy-zone the easier path available for the shrinkage flow over the mushy-zone. Therefore, in Al-19Cu grown at 10 μm/s with the most steepled mushy-zone the effect of area-change-driven-shrinkage flow is hardly seen, but in the Al-7Si grown at 29.1 μm/s, with the least steepled mushy-zone, area-change-driven-shrinkage flow has no choice but to go into the mushy-zone changing the parabolic radial macrosegregation profile to *S*-shape in deeper locations below the contraction neck. Irrespective of the nature of the alloy or the growth

speed, almost no radial macrosegregation was seen in the smaller diameter portion of the samples close to the contraction.

3. Directional solidification through an abrupt cross-section increase: Since the area-change-induced shrinkage flow effects are minimal during cross-section increase (larger cross-section area liquid column is feeding solidification shrinkage in the smaller area portion below), this flow is not expected to influence the longitudinal macrosegregation in the vicinity of section increase. However, simulations and experiments both showed a negative macrosegregation right on the expansion platform. This is because the secondary branches of emerging primary dendrites from below expand side-ways to fill the larger area cavity immediately after the expansion forming almost a continuous layer of solute poor α-phase on the shelf, and also due to the freezing of the preexisting C_0 liquid on the expansion shelf.

   The mushy-zone traversing in the 3.5 mm diameter constant cross-section portion of the mold below develops a steepled mushy-zone commensurate with solidification conditions there. However, contrary to the cross-section decrease situation summarized above, where the intensified shrinkage flow flattened the mushy-zone, here the mushy-zone becomes more steepled right before the expansion, because of a decrease in the solidification shrinkage flow speed (larger area liquid pool feeding solidification shrinkage occurring in the smaller area mold below). This results in creating an increase in the steepness of the parabolic radial macrosegregation profile there. As the already segregated liquid ahead of the mushy-zone exits the expansion, it gets swept outwards by the "steepling convection" attempting to slowly establish its steady-state shape commensurate with the growth conditions in the 9.5 mm constant

cross-section portion of the mold. During this transition, the radial macrosegregation profile instead of being parabolic takes on an *S*-shape profile. The stronger steepling convection in the Al-19Cu grown at 10 μm/s enables its radial macrosegregation profile to transform its *S*-shaped profile to the newly acquired steady-state parabolic shape sooner after the expansion, as compared with the weaker steepling flow in the Al-7Si grown at 29.1 μm/s, where the formation of steady-state steeple and the corresponding parabolic radial macrosegregation profiles occurs at distances farther away from the abrupt section increase.

4. Spurious grain formation during directional solidification involving cross-section increase:

Misoriented spurious grains were observed to form extensively in the Al-19Cu alloy samples; they were not seen in the Al-7Si alloys. The grains appear to form and grow from the reentrant corners of the expansion shelf and not at the outer edges of the platform. This is contrary to the observations reported in the literature in superalloy gas-turbine blade components directionally solidified in constant wall thickness ceramic molds. Our experimental observations support solutal remelting and fragmentation of slender "tertiary-branches" due to thermosolutal convection as the main mechanism for the formation of spurious grains during directional solidification involving a section increase. A parameter proposed by Mehrabian [46] ($\frac{v.\nabla T}{\varepsilon} < -1$) shows a very good correlation between the experimentally observed spurious grain formation behavior in these alloys and that expected from the interactions among the various convective flows associated with the cross-section increase. As the mushy-zone is exiting the expansion, solute-rich liquid from around the periphery of the

narrow portion of the mold gets in contact with side-branches growing to fill the larger diameter cavity above; delicate secondary and tertiary branches are prone to remelting and fragmentation in this region. Broken primary α-phase solids in Al-19Cu are very likely to float up ahead of the mushy-zone because their density is lower than the melt surrounding them; therefore, provided the local thermal conditions allow, they can grow and develop into spurious grains. The likelihood of such dendrite fragmentation is less in Al-7Si samples grown under similar condition than Al-19Cu, because the thermosolutal convection is less intense in Al-7Si; in addition even if dendrite fragments form, the will not float but sink (because they are heavier than the liquid phase around them) and will get entrapped into the growing dendritic array. Therefore, spurious grain formation due to solutal remelting and fragmentation is much more likely to happen in the Al-19Cu alloys solidifying out of a cross-section expansion than in Al-7Si growing in similar condition as is observed in this research.

5. Nearest Neighbor Spacing and Primary Dendrite Trunk Diameter:

The Nearest Neighbor Spacings (NNS) measured on several transverse microstructure of both alloys, during area contraction and also expansion, did not show any special behavior associated with the cross-section change. Their values were found to be less than those predicted from the theoretical models, which only account for the diffusion transport. This supports the previous observation that "steepling convection" decreases primary dendrite spacing. Trunk Diameter (TD) appears to respond more readily to the changes in the growth conditions; slower grown samples showed larger trunk diameter in agreement with expectations from a recently proposed theoretical

model [57]. Also, the Al-7Si samples grown at similar condition to Al-19Cu showed larger trunk diameter.

Chapter V

Proposed Future Research

Low gravity directional solidification is required to more meticulously examine the role of convection in macrosegregation and in morphological properties of dendritic array. In the absence of gravity force, no steepling thermosolutal convection happens; therefore, the effect of section-change-induced shrinkage flow could be isolated and studied. Directional solidification through contraction will produce a relatively strong shrinkage flow, whereas for the area expansion this effect will be minimal.

Additional experiments, involving gentle cross-section increase, instead of abrupt change as studied here, will be helpful in understanding the effect of geometry transition on the radial and longitudinal macrosegregation, and also on the formation of spurious grains.

In this work, the area ratio of the smaller to the larger sections was seen to be determinative of the radial macrosegregation profile in the larger diameter sections both before contraction and after expansion. Therefore, further experiments with varying area

ratios may be quite valuable in understanding the effect of area-change during directional solidification of metallic alloys on the radial and axial macrosegregation.

And finally, it is imperative that more realistic 3-dimenional numerical models be developed and used to simulate the interaction between the solidifying mushy-zone and the thermosolutal transport occurring during the directional solidification of metallic alloys through cross-section changes.

References

[1] M. Flemings, Solidification Processing, McGraw-Hill, 1974.

[2] E. Scheil, “Bemerkungen zur schichtkristallbildung (retrograde saturation curves),"Zeitschrift fur Metallkunde, vol. 34, pp. 70-72, 1942.

[3] G. H. Gulliver, Metallic Alloys, pp. 206-210. London, UK: Griffn, 1922.

[4] R. C. Reed, The Superalloys, p. 139. Cambridge, UK: Cambridge Univ. Press, 2006.

[5] M. Flemings and G. Nereo, "Macrosegregation: Part I," Trans. TMS-AIME, vol. 239, p. 1449, 1967.

[6] M. Flemings, R. Mehrabian and G. Nereo, "Macrosegregation: Part II," Trans. TMS-AIME, vol. 242, pp. 41-49, 1968.

[7] M. Flemings and G. Nereo, "Macrosegregation: Part III," Trans. TMS-AIME, vol. 242, pp. 50-55, 1968.

[8] S. Tewari, R. Shah and M. Chopra, "Thermosolutal Convection and Macrosegregation Caused by Solute Rejection at Cell/Dendrite Tips," Metall. Mater. Trans. A, vol. 24A, no. 7, 1993.

[9] S. Tewari and R. Shah, "Macrosegregation During Dendritic Array Arrayed Growth of Hypoeutectic Pb-Sn Alloys: Influence of Primary Arm Spacing and Mushy Zone Length," *Metall. Mater. Trans. A*, vol. 27A, no. 5, 1996.

[10] H. Dong, H. Dai, J.-C. Geblin, M. Newell, R. Reed, N. D'Souza and P. Brown, "Grain Selection during Solidification in Spiral Grain Selector," Journal of the Minerals, Metals and Materials Society, pp. 367-374, 2008.

[11] M. Burden, D. Hebditch, and J. Hunt, "Macroscopic stability of a planar, cellular or dendritic interface during directional freezing," Journal of Crystal Growth, vol. 20, no. 2, pp. 121-124, 1973.

[12] D. McCartney and J. Hunt, \Measurements of cell and primary dendrite arm spacings in directionally solidified aluminium alloys," Acta Metallurgica, vol. 29, no. 11, pp. 1851-1863, 1981.

[13] J. T. Mason, J. D. Verhoeven, and R. Trivedi, "Primary dendrite spacing: part II. experimental studies of Pb-Pd and Pb-Au alloys," Metallurgical and Materials Transactions A, vol. 15, no. 9, pp. 1665_1676, 1984.

[14] J. D. Verhoeven, J. T. Mason, and R. Trivedi, "The effect of convection on the dendrite to eutectic transition," Metallurgical and Materials Transactions A, vol. 17, no. 6, pp. 991-1000, 1986.

[15] H. Nguyen Thi, Y. Dabo, B. Drevet, M. Dupouy, D. Camel, B. Billia, J. Hunt, and A. Chilton, "Directional solidification of Al-1.5wt%Ni alloys under diffusion transport in space and fluid-flow localisation on earth," Journal of Crystal Growth, vol. 281, no. 2-4, pp. 654-668, 2005.

[16] B. Billia, H. N. Thi, G. Reinhart, Y. Dabo, B. H. Zhou, Q. S. Liu, T. Lyubimova, B. Roux, and C. W. Lan, "Tailoring of dendritic microstructure in solidification processing

by crucible vibration/rotation," Microgravity – Science and Technology, vol. 16, no. 1-4, pp. 15-19, 2005.

[17] S.R. Coriell, B.T. Murray, A.A. Chernov and G.B. McFadden, Effects of shear flow and anisotropic kinetics on the morphological stability of a binary alloy, Metall. Mater. Trans. A 27A, 687 (1996).

[18] T. Huang, S. Liu, Y. Yang, D. Lu and Y. Zhou, Coupling of coquette flow and crystal
morphologies in directional freezing, J. Cryst. Growth 128, 167 (1993).

[19] T. Huang, L. Deyang and Z. Yaoche, Diffusion convection effects on constrained dendritic growth in dilute alloys, Acta Astronautica,12[9], 997 (1988).

[20] H. Esaka, T. Taenaka, H. Ohishi, S. Mizoguchi and K. Kajikoa, A model experiment for
solidification-deflection mechanism of primary dendrite due to fluid flow, International Symposium on Scale Modeling, July 18-22, 1988, Tokyo, The Japan Society of Mechanical Engineers, pp. 287-293 (1988).

[21] T. Okamoto, K. Kishitake and I. Bessho, Dendritic structure in unidirectionally solidified cyclohexanol, J. Cryst. Growth 29, 131 (1975).

[22] B. Drevet, H. Nguyen Thi, D. Camel, B. Billia and M.D. Dupouy, Solidification of aluminum lithium alloys near the cell/dendrite transition- influence of solutal convection, J. Cryst. Growth 218, 419 (2000).

[23] M.D. Dupouy, D. Camel and J.J. Favier, Natural convection in directional dendritic solidification of metallic alloys: dendritic array primary spacing, Acta Metall. 40 [7], 1791 (1992).

[24] L. Yu, G.L. Ding, S.N. Ojha and S.N. Tewari, Mushy zone morphology during directional solidification of Pb-5.8 wt% Sb alloy, Metall. Mater. Trans. A 31A2275 (2000).

[25] T.S. Piwonka and P.N. Atanmo, Multicomponent macrosegregation in a vacuum melted
unidirectionally solidified superalloy, in Vacuum Metallurgy, Proceedings of Vacuum Metallurgy Conference, Pittsburgh, June 20-22, 1977, 507.

[26] R. Sellamuthu, M.S. Thesis. University of Pittsburgh, Pittsburgh, PA (1979).

[26] W,-C.S. Wang, M.S. Thesis, The University of Arizona, Tucson, Arizona (1983).

[28] S.D. Felicelli, D.R. Poirier and J.C. Heinrich, Macrosegregation patterns in multicomponent Ni base alloys, J. Cryst. Growth 177, 145 (1997).

[29] S.D. Felicelli, J.C. Heinrich and D.R. Poirier, Finite element analysis of directional solidification of multicomponent alloys, Int.J. Num. Meth. Fluids 27, 207 (1998).

[30] M. Rappaz, Ch.-A. Gandin, J.-L. Desbiolles, and ph. Thevoz, Predictions of grain structures in various solidification processes. Metall. Mater. Trans. A, 27A, 695 (1996).

[31] H. Hao, W. Jiang, G. Xie, G. Zhang, Y. Lu, J. Zhang and L. Lou, Microstructure and grain orientation evolution of a specially shaped shroud during directional solidification process, Progress in Natural Science: Materials International 23[2], 211 (2013).

[32] D. Ruvalcaba, R.H. Mathiesen, D.G. Eskin, L. Arnberg and L. Katgerman: Observations of dendritic fragmentation due to local solute enrichment during directional solidification of an aluminum alloy, *Acta. Mater.* **55**, 4287 (2007).

[33] D. Ma, J. Ziehm, W. Wang and A. Buhrig-Polaczek, Freckle formation in directionally solidified superalloy components with expanding cross-section. The 3rd

International Conference on Advances in Solidification Processes, *IOP Conference Series: Mater. Sci. Eng.* **27**, 2011, 012034.

[34] L.M. Fabietti, V. Seetharaman and R. Trivedi, Development of solidification microstructures in the presence of lateral constraints. Metall. Transa. A, 21A, 1299 (1990).

[35] D. Poirier, "Transport and thermodynamic properties for solidification of Al-7Si alloy." The University of Arizona, Tucson, AZ, Unpublished report, June 2011.

[36] D. R. Poirier, "Density, viscosity, and diffusion coefficients in hypoeutectic Al-Si liquid alloys: an assessment of available data," Metallurgical and Materials Transactions B, pp. 1-10, 2014.

[37] S. Ganesan and D. R. Poirier, "Densities of aluminum-rich aluminum-copper alloys during solidification," Metallurgical Transactions A, vol. 18, no. 5, pp. 721-723, 1987.

[38] Luke Johnson, "Analysis of Microstructure and Macrosegregation for Directional Solidification of Al-7 Wt% Si Alloy with a Cross-Section Change at Growth Speeds of 10 and 29.1 μm/s," Master of Science Thesis, Cleveland State University, Cleveland Ohio, 2013.

[39] M. Ghods, L. Johnson, M. Lauer, R. N. Grugel, S. N. Tewari, D. R. Poirier, J. Cryst. Growth 441 (2016) 107–116.

[40] Gandin, Ch-A., and Michel Rappaz. "A coupled finite element-cellular automaton model for the prediction of dendritic grain structures in solidification processes." Acta Metallurgica et Materialia 42.7 (1994): 2233-2246.

[41] Gandin, Ch-A., et al. "A three-dimensional cellular automation-finite element model for the prediction of solidification grain structures." Metallurgical and Materials Transactions A 30.12 (1999): 3153-3165.

[42] Kermanpur, A., et al. "Thermal and grain-structure simulation in a land-based turbine blade directionally solidified with the liquid metal cooling process." Metallurgical and Materials Transactions B 31.6 (2000): 1293-1304

[43] Mathiesen, R. H., et al. "Crystal fragmentation and columnar-to-equiaxed transitions in Al-Cu studied by synchrotron X-ray video microscopy." Metallurgical and Materials Transactions A 37.8 (2006): 2515-2524.

[44] Kumar, Arvind, and Pradip Dutta. "A Rayleigh number based dendrite fragmentation criterion for detachment of solid crystals during solidification." Journal of Physics D: Applied Physics 41.15 (2008): 155501.

[45] D'souza, N., et al. "Seeding of single-crystal superalloys—Role of constitutional undercooling and primary dendrite orientation on stray-grain nucleation and growth." Metallurgical and Materials Transactions B 36.5 (2005): 657-666.

[46] Mehrabian, R., M. Keane, and M. C. Flemings. "Interdendritic fluid flow and macrosegregation; influence of gravity." Metallurgical and Materials Transactions 1.5 (1970): 1209-1220.

[47] Ruvalcaba, D., R. H. Mathiesen, D. G. Eskin, L. Arnberg, and L. Katgerman. "In situ observations of dendritic fragmentation due to local solute-enrichment during directi onal solidification of an aluminum alloy." Acta Materialia 55, no. 13 (2007): 4287-4292.

[48] Mathiesen, R. H., L. Arnberg, P. Bleuet, and A. Somogyi. "Crystal fragmentation and columnar-to-equiaxed transitions in Al-Cu studied by synchrotron X-ray video microscopy." Metallurgical and Materials Transactions A 37, no. 8 (2006): 2515-2524.

[49] Magnusson, T., and L. Arnberg. "Density and solidification shrinkage of hypoeutectic aluminum-silicon alloys." Metallurgical and Materials Transactions A 32, no. 10 (2001): 2605-2613.

[50] J. Hunt and S. Lu, "Numerical Modeling of Cellular/Dendritic Array Growth: Spacing and Structure Predictions," Metall. Mater. Trans. A, vol. 27A, pp. 611-623, 1996.

[51] W. Kurz and D. Fisher, "Dendritic Growth at the Limit Stability of Tip Radius and Spacing," Acta Metall., vol. 29, p. 11, 1981.

[52] R. Trivedi, "Interdendritic Spacing 2: A Comparison of Theory and Experiment," Metall. Trans. A, vol. 15A, p. 977, 1984.

[53] J. Hunt and S. Lu, "A Numerical Analysis of Dendritic and Cellular Array Growth: The Spacing Adjustment Mechanisms," Journal of Crystal Growth, vol. 123, pp. 17-34, 1992.

[54] D. Poirier, P. Zhao and J. Heinrich, "Dendritic Solidification of Binary Alloys with Free and Forced Convection," Int. J. Numer. Meth. Fluids, vol. 49, pp. 233-266, 2005.

[55] N. Al-Rawahi and G. Tryggvason, "Numerical Simulation of Dendritic Solidification with Convection: Three-Dimensional Flow," J. Comp. Physics, vol. 194, pp. 677-696, 2004.

[56] R. Katz and M. Worster, "Simulation of Directional Solidification, Thermochemical Convection, and Chimney Formation in a Hele-Shaw Cell," J. Comp. Physics, vol. 227, pp. 9823-9840, 2008.

[57] Tewari, S. N., R. N. Grugel, and David R. Poirier. "An evaluation of primary dendrite trunk diameters in directionally solidified Al-Si alloys." Metallurgical and Materials Transactions A 45, no. 11 (2014): 4758-4761.

[58] Kirkwood, D. H. "A simple model for dendrite arm coarsening during solidification." Materials Science and Engineering 73 (1985): L1-L4.

Appendices

Appendix A:

```
clc; clear all
ExcelFile= uigetfile;
raw=xlsread(ExcelFile);  %% the numerical values of the excel file will
sit in a matrix called raw
[r c]=size(raw);  % r is number of rows and c is number of columns in
data excel file
scale=2420;  % number of pixels per mm in original image

%%% the for loop scans pairs of line in the "raw" matrix
for n=1:r/2

    % this if takes care of the regular drwan lines. The sixth element
of
    % each row is the angle and the decision about the use of BX and BY
as a known point
    % on the drawn line is based on this angle value


    if ((raw(2*n-1,6)<0) && (raw(2*n-1,6)> -90)) || ((raw(2*n-1,6)> 90)
&& (raw(2*n-1,6)< 180))
        X1=raw(2*n-1,2);
        Y1=raw(2*n-1,3);
        X2=raw(2*n,2);
        Y2=raw(2*n,3)+raw(2*n,5);
        m1=-tand(raw(2*n-1,6));
        m2=-tand(raw(2*n,6));
        X=(m1*X1-Y1+Y2-m2*X2)/(m1-m2);
        Y=m1*(X-X1)+Y1;
        TD=(raw(2*n-1,7)+raw(2*n,7))/2/(scale/1000);

    else if ((raw(2*n-1,6)<90) && (raw(2*n-1,6)> 0)) || ((raw(2*n-1,6)>
-180) && (raw(2*n-1,6)< -90))
        X1=raw(2*n-1,2);
        Y1=raw(2*n-1,3)+raw(2*n-1,5);
        X2=raw(2*n,2);
        Y2=raw(2*n,3);
        m1=-tand(raw(2*n-1,6));
        m2=-tand(raw(2*n,6));
        X=(m1*X1-Y1+Y2-m2*X2)/(m1-m2);
        Y=m1*(X-X1)+Y1;
        TD=(raw(2*n-1,7)+raw(2*n,7))/2/(scale/1000);
        end
    end

    %%%%%% special cases start here %%%%%%%%

    % this if makes decision about the use of BX and BY in case the
first line in a pair is vertical
```

```
    % and the second one is either in first or in third quadrant
    if ((raw(2*n-1,6)== 90) || (raw(2*n-1,6)== -90)) &&
(((raw(2*n,6)<90) && (raw(2*n,6)> 0)) || ((raw(2*n,6)> -180) &&
(raw(2*n,6)< -90)))
    X2=raw(2*n,2);
    Y2=raw(2*n,3)+raw(2*n,5);
    m2=-tand(raw(2*n,6));
    X=raw(2*n-1,2);
    Y=m2*(X-X2)+Y2;
    TD=(raw(2*n-1,7)+raw(2*n,7))/2/(scale/1000);
    end

    % this if makes decision about the use of BX and BY in case the
first line in a pair is vertical
    % and the second one is either in forth or in second quadrant
    if ((raw(2*n-1,6)== 90) || (raw(2*n-1,6)== -90)) &&
(((raw(2*n,6)<0) && (raw(2*n,6)> -90)) || ((raw(2*n,6)> 90) &&
(raw(2*n,6)< 180)))
    X2=raw(2*n,2);
    Y2=raw(2*n,3);
    m2=-tand(raw(2*n,6));
    X=raw(2*n-1,2);
    Y=m2*(X-X2)+Y2;
    TD=(raw(2*n-1,7)+raw(2*n,7))/2/(scale/1000);
    end

    % this if makes decision about the use of BX and BY in case the
first
    % line in a pair is horizontal
    % and the second one is either in first or in third quadrant
    if ((raw(2*n-1,6)== 0) || (raw(2*n-1,6)== 180)) &&
(((raw(2*n,6)<90) && (raw(2*n,6)> 0)) || ((raw(2*n,6)> -180) &&
(raw(2*n,6)< -90)))
    X2=raw(2*n,2);
    Y2=raw(2*n,3)+raw(2*n,5);
    m2=-tand(raw(2*n,6));
    Y=raw(2*n-1,3);
    X=(Y-Y2)/m2+X2;
    TD=(raw(2*n-1,7)+raw(2*n,7))/2/(scale/1000);
    end

    % this if makes decision about the use of BX and BY in case the
first
    % line in a pair is horizontal
    % and the second one is either in forth or in second quadrant
    if ((raw(2*n-1,6)== 0) || (raw(2*n-1,6)== 180)) && (((raw(2*n,6)<0)
&& (raw(2*n,6)> -90)) || ((raw(2*n,6)> 90) && (raw(2*n,6)< 180)))
    X2=raw(2*n,2);
    Y2=raw(2*n,3);
    m2=-tand(raw(2*n,6));
    Y=raw(2*n-1,3);
    X=(Y-Y2)/m2+X2;
    TD=(raw(2*n-1,7)+raw(2*n,7))/2/(scale/1000);
    end
```

```
    % this if makes decision about the use of BX and BY in case the
first
    % line in a pair is horizontal
    % and the second one is vertical
    if ((raw(2*n-1,6)== 0) || (raw(2*n-1,6)== 180)) && ((raw(2*n,6)==
90) || (raw(2*n,6)== -90))
    X=raw(2*n,2);
    Y=raw(2*n-1,3);
    TD=(raw(2*n-1,7)+raw(2*n,7))/2/(scale/1000);
    end

    % this if makes decision about the use of BX and BY in case the
first
    % line in a pair is vertical
    % and the second one is horizontal
    if ((raw(2*n-1,6)== 90) || (raw(2*n-1,6)== -90)) && ((raw(2*n,6)==
0) || (raw(2*n,6)== 180))
    X=raw(2*n-1,2);
    Y=raw(2*n,3);
    TD=(raw(2*n-1,7)+raw(2*n,7))/2/(scale/1000);
    end


    % putting the calculated X and Y corresponding to center of
dendrite
    % and its trunk diameter in proper place in result matrix
    result(n,2)=X;
    result(n,3)=Y;
    result(n,4)=TD;

end


% this loop calculates NNS, 3NNS and 6NNS based on calculated X and Y
of each dendrite
% it starts from the first point in the table and calculates the
distances from that point to all other poins, then sorts
% the distances vector and selects the first element as NNS, mean of
first
% three as 3NNS and mean of first six as 6NNS
for i=1:r/2
    z=1;
   for j=1:r/2
      if i~=j %
         distance(z)=sqrt((result(i,2)-(result(j,2)))^2+(result(i,3)-
(result(j,3)))^2);
         z=z+1;
      end
   end
    distance=sort(distance);
    NNS(i)=distance(1);
    NNS3(i)=mean(distance(1:3));
    NNS6(i)=mean(distance(1:6));

end
```

```
% converting spacings to micro meter
NNS=(NNS./(scale/1000))';
NNS3=(NNS3./(scale/1000))';
NNS6=(NNS6./(scale/1000))';

if (r/2)>= 15

    NNS_s=sort(NNS);
    top10_NNS_avg=mean(NNS_s(1:round((r/2)/10)));
    top10_NNS_std=std(NNS_s(1:round((r/2)/10)));
    bott10_NNS_avg=mean(NNS_s(length(NNS_s)-round((r/2)/10)+1:end));
    bott10_NNS_std=std(NNS_s(length(NNS_s)-round((r/2)/10)+1:end));

    TD=sort(result(:,4));
    top10_TD_avg=mean(TD(1:round((r/2)/10)));
    top10_TD_std=std(TD(1:round((r/2)/10)));
    bott10_TD_avg=mean(TD(length(TD)-round((r/2)/10)+1:end));
    bott10_TD_std=std(TD(length(TD)-round((r/2)/10)+1:end));

end

% calculating the mean and standard deviation on spacing for the whole
data
% set
NNS_Mean=mean(NNS);
NNS_STD=std(NNS);
NNS3_Mean=mean(NNS3);
NNS3_STD=std(NNS3);
NNS6_Mean=mean(NNS6);
NNS6_STD=std(NNS6);

% putting calculated spacings in the results table
result(:,5)=NNS;
result(:,6)=NNS3;
result(:,7)=NNS6;
result(:,1)=1:r/2; % filling the first column of result table with
dendrites numbers

% creating output excel file
filename = 'XY_TD_PDAS.xlsx';
A = {'Dendrite No.','Dendrite Center X','Dendrite Center Y','Dendrite
TD(um)','Dendrite NNS(um)','Dendrite 3 NNS(um)','Dendrite 6 NNS(um)'};
xlswrite(filename,A,1)
xlRange = 'E1';
xlswrite(filename,result,1,'A2')

if (r/2)>= 15
    B={'TD mean','TD std','NNS mean','NNS std',...
        'Top 10% TD avg','Top 10% TD std','bottom 10% TD avg','bottom
10% TD std',...
        'Top 10% NNS avg','Top 10% NNS std','bottom 10% NNS
avg','bottom 10% NNS std'};
```

```
    xlswrite(filename,B,1,'J3')

xlswrite(filename,[mean(result(:,4)),std(result(:,4)),mean(result(:,5))
,std(result(:,5)),...
        top10_TD_avg,top10_TD_std,bott10_TD_avg,bott10_TD_std...

top10_NNS_avg,top10_NNS_std,bott10_NNS_avg,bott10_NNS_std],1,'J4')

else
    B={'TD mean','TD std','NNS mean','NNS std'};
    xlswrite(filename,B,1,'J3')

xlswrite(filename,[mean(result(:,4)),std(result(:,4)),mean(result(:,5))
,std(result(:,5))],1,'J4')

end
```

Appendix B

In the model used, the difference between the density of the solid phase, ρ_s, and liquid phase, ρ_l, in the continuity equation shown below as equation (b1), accounts for the shrinkage flow. In this equation ϕ is the volume fraction liquid and **u** is the liquid velocity.

$$(\rho_l - \rho_s)\frac{\partial \phi}{\partial t} + \rho_l \boldsymbol{\nabla} . \mathbf{u} = 0 \quad \text{(b1)}$$

Boussinesq approximation of the liquid density in the momentum equation below (b2), which includes thermal and solutal effects, $\rho^* = \rho_l\left[1 + \beta_T\left(T - T_{ref}\right) + \beta_C(C_l - C_{ref})\right]$, captures the thermosolutal convection. The permeability model used is a tensor, **K,** with one component perpendicular and one parallel to the direction of solidification. The experimentally measured primary dendrite arm spacing together with liquid volume fraction, calculated at each iteration of simulation, are used to obtain the local permeability.

$$\frac{\partial \boldsymbol{u}}{\partial t} + \frac{\boldsymbol{u}}{\phi}.\nabla \mathbf{u} - \frac{\rho_s - \rho_l}{\rho_l \phi}\frac{\partial \phi}{\partial t}\boldsymbol{u} = -\frac{\phi}{\rho_l}\boldsymbol{\nabla} p + \frac{\rho^* \phi}{\rho_l} g + \nu\left[\boldsymbol{\nabla}^2 \mathrm{u} - \phi \mathbf{K}^{-1}.\mathbf{u} + \frac{\rho_s - \rho_l}{3\rho_l}\boldsymbol{\nabla}\frac{\partial \phi}{\partial t}\right] \quad \text{(b2)}$$

The solute conservation equation used is shown in equation (b3) below where C_l is the liquid concentration, $D_l$is the diffusivity of solute in the liquid, and $\overline{\rho C} = \rho_s(1-\phi)\bar{C}_s + \rho_l \phi C_l$is the overall solute content with $\bar{C}_s = \frac{1}{1-\phi}\int_{\phi}^{1} k C_l d\phi$ being the average concentration in the solid.

$$\frac{\partial \overline{\rho C}}{\partial t} + \rho_l \boldsymbol{u} . \boldsymbol{\nabla} C_l = \rho_l \left[-\frac{\rho_s - \rho_l}{\rho_l} C_l \frac{\partial \phi}{\partial t} + \boldsymbol{\nabla} . \phi D_l \boldsymbol{\nabla} C_l\right] \quad \text{(b3)}$$

Phase diagram dictates the local thermodynamic equilibrium in the interdendritic liquid of the mushy-zone. In this work, the phase diagram is linearized and the interdendritic liquid concentration is given by $C_l = \frac{T - T_M}{m_l}$ where $T$is the local temperature, $T_M$is linearized melting point of pure aluminum, and $m_l$is the phase diagrams liquidus slope.

Equation (b4) below is the energy equation used in the simulations in which $\overline{\rho c_p} = \rho_s(1-\phi)c_{ps} + \rho_l \phi c_{pl}$, and $c_{ps}$and $c_{pl}$are solid and liquid heat capacities. In the mold only the energy equation is applied, and the second and third terms of the left-hand side of the equation (b4) are ignored; graphite properties are used in the energy equation in the mold.

$$\overline{\rho c_p}\frac{\partial T}{\partial t} + \rho_s\left[\left(c_{ps} - c_{pl}\right) - \left(T_{ref} - T\right) + L\right]\frac{\partial \phi}{\partial t} + \rho_l c_{pl}\mathbf{u}\,.\,\boldsymbol{\nabla} T = \nabla\,.\,(\kappa \boldsymbol{\nabla} T) \qquad \text{(b4)}$$

The two-dimensional simulation domain was meshed using Cartesian quadrilateral elements, and the meshes were refined near the edges of the crucible and at the change in cross-section. Temperature profiles, recorded by thermocouples in the experiments, are applied to the outer perimeter of the mold as a function of time and position with the mold included in the computational domain.